Journal of Healthcare Engineering

Multisensor-Based Activity Recognition in Healthcare Systems

Lead Guest Editor: Atiqur R. Ahad
Guest Editors: João M. Tavares and Belayat Hossain

Multisensor-Based Activity Recognition in Healthcare Systems

Journal of Healthcare Engineering

Multisensor-Based Activity Recognition in Healthcare Systems

Lead Guest Editor: Atiqur R. Ahad
Guest Editors: João M. Tavares and Belayat Hossain

Contents

Hindawi
Journal of Healthcare Engineering
Volume 2020, Article ID 6219845, 9 pages
https://doi.org/10.1155/2020/6219845

Research Article

Application of Multispectral Imaging in the Human Tympanic Membrane

Tien Tran Van,[1,2] **Mi Lu Thi Thao**,[1,2] **Linh Bui Mai Quynh**,[1] **Cat Phan Ngoc Khuong**,[1,2] **and Linh Huynh Quang**[1]

[1]*Ho Chi Minh City University of Technology, Faculty of Applied Science, Department of Applied Physics, 268 Ly Thuong Kiet Street, District 10, Ho Chi Minh City 700 000, Vietnam*
[2]*National Key Laboratory of Digital Control and System Engineering, 268 Ly Thuong Kiet Street, District 10, Ho Chi Minh City 700 000, Vietnam*

Correspondence should be addressed to Tien Tran Van; tranvantien@hcmut.edu.vn

Received 8 November 2019; Revised 25 August 2020; Accepted 27 August 2020; Published 21 September 2020

Academic Editor: Belayat Hossain

Multispectral imaging has recently shown good performance in determining information about physiology, morphology, and composition of tissue. In the endoscopy field, many researches have shown the ability to apply multispectral or narrow-band images in surveying vascular structure based on the interaction of light wavelength with tissue composition. However, there has been no mention to assess the contrast between other components in the middle ear such as the tympanic membrane, malleus, and the surrounding area. Using CT, OCT, or ODT can clearly describe the tympanic membrane structure; nevertheless, these approaches are expensive, more complex, and time-consuming and are not suitable for most common middle ear diagnoses. Here, we show the potential of using the multispectral imaging technique to enhance the contrast of the tympanic membrane compared to the surrounding tissue. The optical absorption and scattering of biological tissues constituents are not the same at different wavelengths. In this pilot study, multiwavelength images of the tympanic membrane were captured by using the otoscope with LED light source at three distinct spectral regions: 450 nm, 530 nm, and 630 nm. Subsequently, analyses of the intensity images as well as the histogram of these images point out that the 630 nm illumination image features an evident contrast in the intensity of the tympanic membrane and malleus compared to the surrounding area. Analysis of such images could facilitate the boundary determination and segmentation of the tympanic membrane (TM) with high precision.

1. Introduction

Nowadays, multispectral imaging (MSI) techniques have more and more applications in medical and surgical diagnostics. A multispectral image is a collection of several monochrome images on the same object within specific wavelength ranges. The absorption and reflection of each tissue type are not the same at different wavelengths, and the interaction of light with tissue will fully describe the characteristics of tissue. In the field of dermatology, MSI in visible spectrum has been used to map the distribution of hemoglobin and melanin in skin surface [1, 2] and detect skin cancer lesions [3]. In many other fields, such as gastroenterology and gynecology, MSI techniques have also achieved promising results in tissue observation and become a new diagnosis tool to identify human diseases [4, 5].

In human ear, the application of MSI was first studied by Valdez et al. Photos of TM and its surrounding region were taken with otomicroscopy using multichannel LED light source [6]. This result showed that combining blue with green or white light offered much better details of the blood vessel's pattern [6]. In addition, they also proposed that the images taken under red and near-infrared light illumination can be used for detection of pus and infected fluid which accumulate in otitis media [6, 7], in which middle ear infections, also called otitis media, is one of the most common inflammations in children, caused by infection of ear tissue, including the TM and tissues behind it [8]. To diagnose otitis

media, most physicians observe blood vessel distribution in the TM as well as the changes of the TM (color, location, mobility of the TM) by using otoscope or endoscopy with white light source. However, determining the changing of TM is not easy for the younger children with the smaller and narrower canals and acute otitis media is the most common in this age group. The early detection and treatment of otitis media can prevent two major problems of complications (such as meningitis, ear infection, and bone necrosis) and hearing loss [8]. Moreover, accurate determination of the TM is also important in case of cochlear implant surgery [9, 10].

Accurate determination of the TM is necessary for correct diagnosis of otitis media. Recently, some researches have developed more algorithms for evaluation or segmentation of TM using endoscope images [11–13]. The first mentioned research is the study of Xie et al. [11]; they used a geometric snake to detect abnormalities in otoscope images. Although this method detected the defects successfully, the elimination of glare might cause the malleus to be lost while it is an important component of the TM. Kuruvilla et al. have developed an algorithm to diagnose the otitis media relying on the TM changes of color, position, and translucence with an accuracy of 89.9% after comparing with the physicians [12]. On the other hand, machine-learning method is also increasingly used in diagnosis of middle ear diseases [14, 15]. Seok et al. show that it is difficult to delineate the exact boundary of the TM; accuracy of TM detection was only 80% when an intersection over union (IoU) score of greater than 0.8 was used [14]. Başaran et al. also used the CNN model and recognized the TM with an average precision of 75.85% [15]. These studies almost used ear endoscopy with white light illumination; however, there are some challenges in brightness and contrast as the lighting, which led to irregularly light fields, and the low contrast of the boundaries in anatomical structures makes automatically structural recognition or segmentation difficult [11–15].

In this study, a traditional endoscope was used to capture the images of the reflection of light from the eardrum. Light source was upgraded to high luminance multispectral LEDs with three distinct spectral regions, blue light (450 nm), green light (530 nm), and red light (630 nm), and cold white light (~6000 K). The absorption properties and depth penetration capacity of different wavelengths in each type of tissue allowed us to improve flexibly images specific for TM, malleus, or blood vessel. Similar approaches have been reported [6]; however, they used otoscope and focused on enhancing the contrast of blood vessels using blue and green spectrum. Here, we focus on the analysis of the image of eardrum captured under red light. Then, the multispectral imaging of human TM was processed by active contour algorithms built on Matlab platform to detect the TM. The segmentation result was analyzed by ENT experts and evaluated by reliable parameters (the Dice similarity coefficient and the Hausdorff distance value).

2. Materials and Methods

2.1. Optical System Description. A traditional optical endoscope was upgraded with multiwavelength LED light source (see Figure 1). First, endoscope LED RGB light source (Cree manufacturer) with light intensity can be adjusted with a control switch. Next, a fiber optic cable with 2.5 mm diameter and 230 cm long and a rigid endoscope (Provix, Korea) with 2.7 mm diameter and 110 mm long were used to lead the light. To connect the rigid endoscope and camera, an optical C mount coupler for endoscope camera adapter focal length F20 is used. A color CCD camera (Edmund Optics) with a resolution of 976×494 pixels is chosen to capture the images and a computer is used for storage and image processing.

2.2. Volunteers. The study was approved by the Institutional Evaluation Council of Vietnam National University, Ho Chi Minh City, and conducted according to the principles of the Helsinki Declaration. During the study, we conducted data collection from 12 volunteers, aged 19 to 22 years; the percentage of men and women is equal (Table 1). The middle ear images were taken on both sides of the ear and did not appear to be pathological. Of these 12 sets of images, 7 sets contain blood vessels and the remaining 5 sets have no presence of blood vessels on the tympanic membrane. In Figure 2, a case of normal eardrum was captured using white light. The TM is primarily conical in shape with the apex forming an umbo. The pars flaccida can be identified above the short process of the malleus, and the pars of tensa locate around the umbo. The cone of light region is the reflection of the light used for examining the ear canal, which appears in the anterior-inferior quadrant near the umbo. Blood vessels appear in the wall of meatus as well as in the malleus.

2.3. Image Segmentation. To segment the TM out of ear canal, active contour algorithm developed by Lankton and Tannenbaum [16] was used. Active contours or snakes are curves and used to define an image domain that can move when it is affected by internal forces coming from the curve itself and external forces computed from the image data. The internal and external forces are defined, so that the snake will conform to an object boundary or other desired features within an image. According to the study of Lankton and Tannenbaum [16], computing these local energies is done with the evolving curve for splitting local neighborhoods into local interior and local exterior. An image is defined on the domain Ω, and let C be a closed contour represented as the zero-level set of a signed distance function φ. The interior of C is specified by the following approximation of the smoothed Heaviside function:

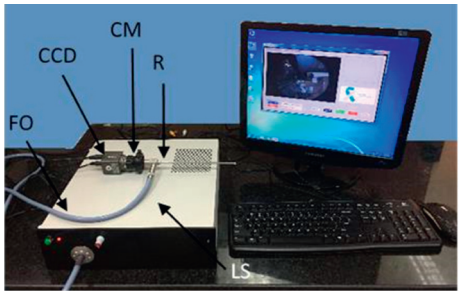

Figure 1: The endoscope model: LS: LED light source and control; R: rigid endoscope; CM: optical C mount coupler; CCD: Color CCD camera; FO: fiber optic cable.

Table 1: Summary of data collection.

Sample	Age (years)	Pathology	Blood vessel	Image(s)
7	19–22	Normal	✓	28
5	19–22	Normal	×	20

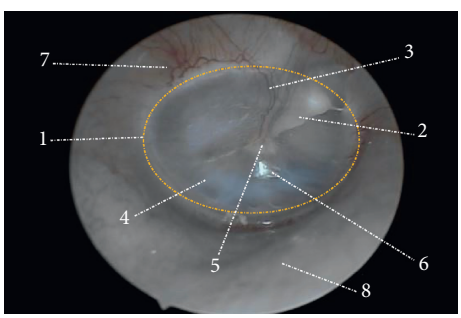

Figure 2: The white image of normal right eardrum was captured using endoscope. 1: TM (orange circle). 2: handle of malleus. 3: pars flaccida. 4: pars of tensa. 5: umbo. 6: cone of light. 7: blood vessel. 8: wall of meatus.

$$\mathcal{H}\varphi(x) = \begin{cases} 1, & \varphi(x) < -\varepsilon, \\ 0, & \varphi(x) > \varepsilon, \\ \frac{1}{2}\left\{1 + \frac{\varphi}{\varepsilon} + \frac{1}{\pi}\sin\left(\frac{\pi\varphi(x)}{\varepsilon}\right)\right\}, & \text{otherwise.} \end{cases} \tag{1}$$

Similarly, the exterior of C is defined as $(1 - \mathcal{H}\varphi(x))$.

To specify the area just around the curve, we will use the derivative of $\mathcal{H}\varphi(x)$, a smoothed version of the Dirac delta:

$$\delta\varphi(x) = \begin{cases} 1, & \varphi(x) = \varepsilon, \\ 0, & |\varphi(x)| < \varepsilon, \\ \frac{1}{2\varepsilon}\left\{1 + \cos\left(\frac{\pi\varphi(x)}{\varepsilon}\right)\right\}, & \text{otherwise.} \end{cases} \tag{2}$$

To determine the accuracy of the segmentation, the algorithm results will be compared to the ground truth by parameters as the Dice similarity coefficient and the Hausdorff distance value.

The Dice similarity coefficient (DSC) described by Zou et al. [17] is used to measure the overlap segmented TM region between the algorithm and the ground truth detected by ENT specialist. The value is determined by the following formula:

$$\text{Dice} = \frac{2|A \cap B|}{|A| + |B|}. \tag{3}$$

Here, A is the result zoned by algorithm and B is the result zoned by expert otoscopists. The DSC value ranges from 0 to 1. A higher DSC value means that the greater the overlap between the two regions, the more reliable the results.

The maximum HD (the Hausdorff distance) is the maximum distance between one point of set A and the nearest point of set B and defined by [18]

$$HD(A, B) = \max(h(A, B), h(B, A)), \tag{4}$$

$$h(A, B) = \max_{a \in A} \min_{b \in B} a - b. \tag{5}$$

$\|\cdot\|$ is the Euclidean distance between a and b that are two points on the boundary of set A and set B.

3. Results and Discussion

A case of a normal tympanic membrane is illustrated in Figure 3. The images are captured using white light illumination (a), red light (b), green light (c), and blue light (d). By direct observation only, it is difficult to distinguish some differences in monocolor image. So these color images (Figures 3(a)–3(d)) were converted into the grayscale images corresponding to Figures 3(e)–3(h). The image obtained using the white light (see Figures 3(a) and 3(e)) have ear details including malleus handle, blood vessels, incus, and cone of light. On the theory of optical absorption, hemoglobin has high absorption in the blue and green regions of the spectrum; therefore, using green and blue light illumination offered much better details of the blood vessels. White light LED has also two regions of spectrum: one narrow peak at blue region and another wide peak at green-yellow region. In our system, the vascularity can be observed clearly in the

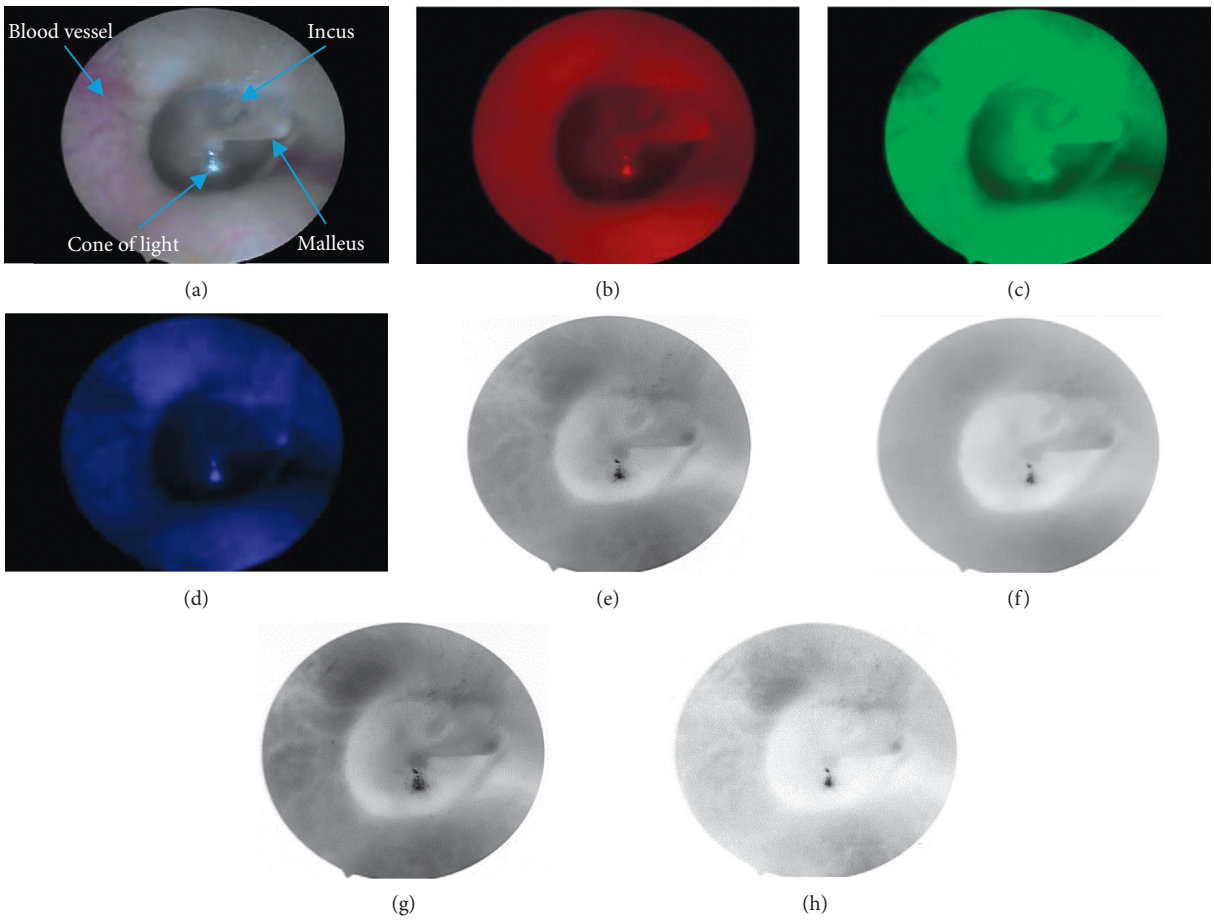

Figure 3: A normal right eardrum: (a) white image, (b) red image, (c) green image, (d) blue image, and (e–h) grayscale images of (a), (b), (c), and (d). (a) White image. (b) Red image. (c) Green image. (d) Blue image. (e) White grayscale image. (f) Red grayscale image. (g) Green grayscale image. (h) Blue grayscale image.

white and green images. The image with blue light affords the lack of illumination in ear cavity which caused identifying poorly the characterization of the TM and blood vessels. This is also leading to create a false boundary and the unsmooth border (see Figure 3(h)).

Our interest here focuses on the absorption in the red light region of the TM and tissues surrounding. First, in the visible spectrum, hemoglobin has the lowest absorption in the region of red light; therefore, the blood vessels did not appear in the red image (see Figures 3(b) and 3(f)). Second, the absorption of collagen is higher than hemoglobin in the red light spectrum [19]. The TM is a thin membrane tissue, consisting of three types of collagen, I, II, and III [20]. Particularly, the middle layers of the pars tensa and annulus are very rich in collagen fibers [21]. Some researchers have shown that red image can be used to express absolute appearance of melanin on the skin [1] or collagen on the breast [19]. Therefore, red image could also be used to produce a high contrast image for collagen structures in the TM. Last, red light penetrates deeper into the tissue than blue and green light. For all of these reasons, the red image has many advantages like increased accuracy of structural identification and functional assessment of the tympanic membrane. The optical characteristic of each tissue type is not the same under different illumination conditions. For more clearly direct observation of the structure of the middle ear, we provide the jet colormap (J) of the multispectral images shown in Figure 3, which is the J white image (a), the J red image (b), the J green image (c), and the J blue image (d) in Figures 4(a)–4(d), respectively. We can see that the distribution of colorscale values on the J white image and the J green image is quite the same; both inside and outside of the tympanic membrane have multiple color levels indicated in Figures 4(a) and 4(c). The J blue image (see Figure 4(d)) is illuminated by a low light source with lots of noise and cannot provide accurate information about the boundary of the tympanic membrane. Interestingly, in the J red image (see Figure 4(b)), there is a significant difference between TM region and the outside of TM region. The handle of malleus appears in the same color as outside of TM. In particular, the outside skin region of the eardrum is relatively homogeneous in component and color and unaffected by noise as other

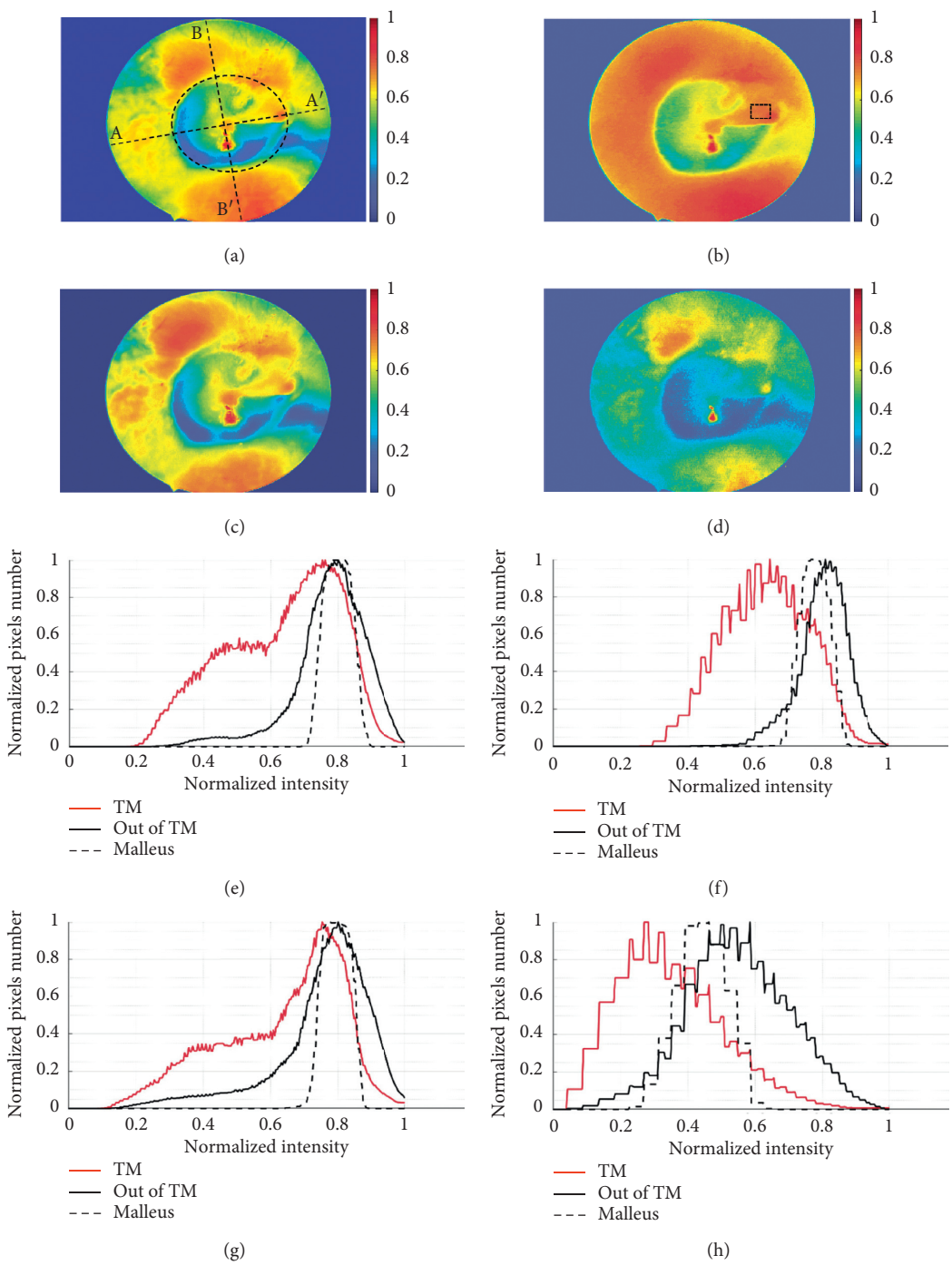

Figure 4: Comparison of intensity images and region histograms obtained with the multispectral imaging on the tympanic membrane shown in Figure 3. (a–d) show the intensity image of white, red, green, and blue image. (e–h) show the region histograms of J white, J red, J green, and J blue image, respectively.

images. Thence, it is possible to distinguish the boundaries of the eardrum and the surrounding area better than the rest of the images.

Next, we offer the region histogram and the line histogram as an evidence to assess the feasibility of detecting TM. First, Figures 4(e)–4(h) show the region histogram maps of the middle ear corresponding to Figures 4(a)–4(d), in which the mean values of TM and wall of meatus (outside of TM) have been measured inside and outside of the ellipse curve as shown in Figure 4(a). A mean value of handle malleus has been measured inside rectangle as shown in Figure 4(b). When superimposing the histograms of J white image and J green image for the TM region and the outside of TM region (wall of meatus), the overlap of two peaks is observed, as shown in Figures 4(e) and 4(g)). The histogram of J blue image also has two very large peaks because of the

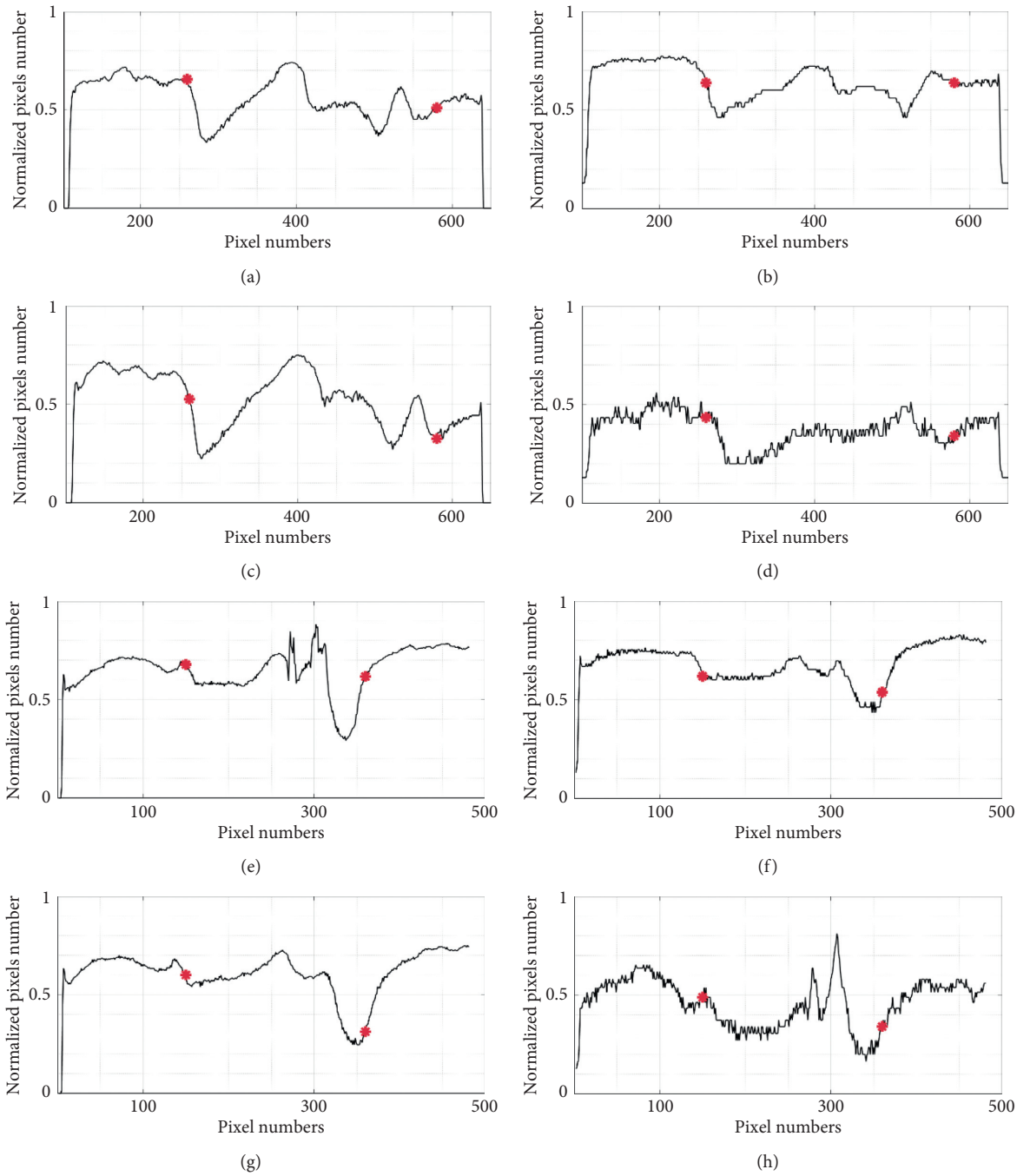

Figure 5: Comparison of the line histogram corresponding to the J white, J red, J green, and J blue image shown in Figure 4. (a–d) the horizontal histogram; (e–h) the vertical histogram.

noise (Figure 4(h)). This is the main reason leading to the inability to segment the TM includes the malleus using threshold-based algorithms. On the other hand, in the region histogram of J red image as shown in Figure 4(f), the overlap of histogram for the inside and outside TM of this image is less than the J white image, J green image, and J blue image. The overlap between the charts is due to the malleus and the wall of the meatus having the same intensity value. The histogram of the outside TM of the J red image has a narrow peak with the homogeneous intensity distribution as can be seen in Figure 4(f). Based on the above results, it is proved that the multispectral imaging can be used to analyze tissue properties of human middle ear and the red image is best suited for identification and segmentation of TM in the middle ear.

In addition, we also provide the line histogram with two special lines (see Figure 4(a)), the first line through the handle of malleus called horizontal line and the second line which is perpendicular to the first line and through the cone of light called vertical line. The intersection of each line (A-

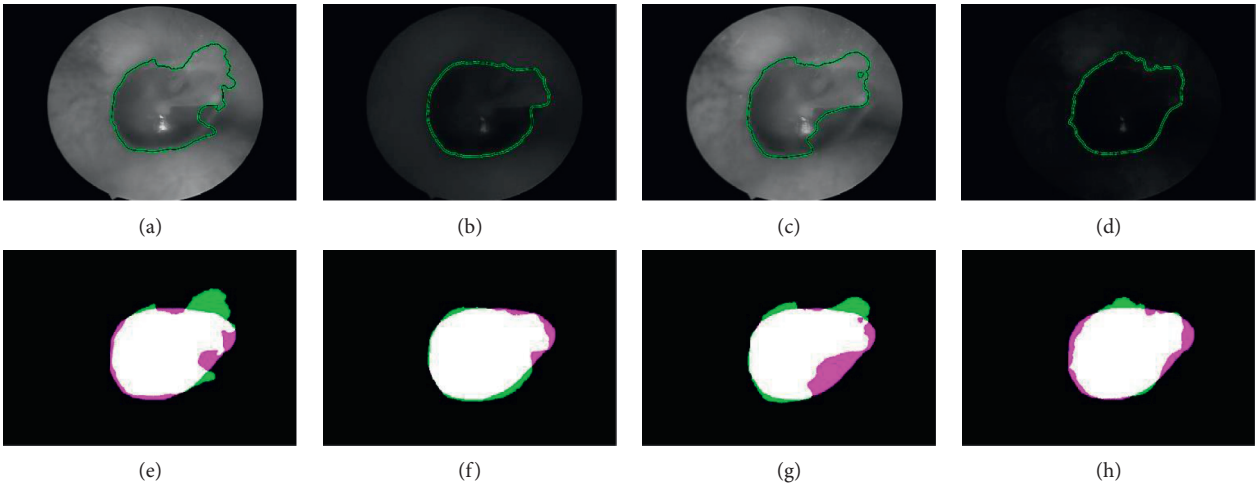

Figure 6: Results of segmentation of the tympanic membrane: (a, e) white, (b, f) red, (c, g) green, and (d, h) blue. Green color is the results of algorithm, pink color is ground truth, and white color is the overlapping.

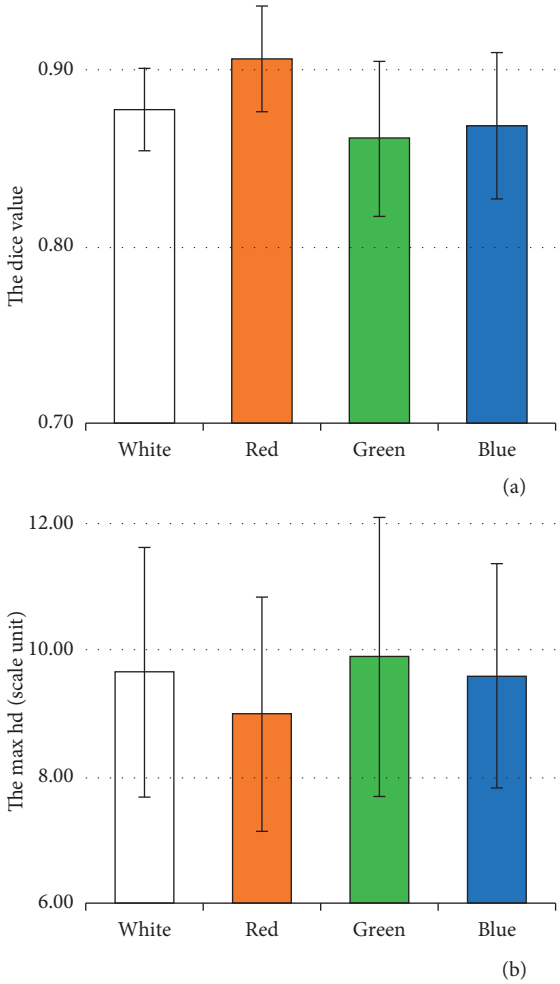

Image	Dice value		
	Mean	1st quartile	3rd quartile
White	0.88 ± 0.02	0.86	0.89
Red	0.91 ± 0.03	0.88	0.92
Green	0.86 ± 0.04	0.82	0.88
Blue	0.87 ± 0.04	0.84	0.89

Image	Maximum HD		
	Mean	1st quartile	3rd quartile
White	9.66 ± 1.97	8.29	10.40
Red	9.00 ± 1.84	6.99	9.83
Green	9.90 ± 2.20	8.19	10.49
Blue	9.59 ± 1.78	8.19	10.50

Figure 7: Average metric values of segmentation results of tympanic membrane: (a) Dice value and (b) max HD.

A′ and B-B′) and ellipse will provide the information of the intensity at the boundary between the TM and the surrounding area. As we can see, the line profiles of Figures 5(a)–5(d) show the strong variation of the intensity at the left boundary and the less change at the right boundary (marked by red dots). This is caused by the malleus attached to the TM, from umbo to the wall of meatus. Besides, the line profiles of Figures 5(e)–5(h) also have strong intensity variations at the upper as well as the under boundary of eardrum (marked by red dots). It proves that using the active contour algorithm is very suitable for the segmentation of the eardrum in this case.

Based on the endoscope device, we proceed to collect 12 series of data of normal TM from volunteers. Each set has four images captured with white, red, green, and blue light and they are completely similar in both size and position of features on the TM. To ensure the stable segmentation result, we choose the white image for putting an ellipse mask which covered the TM and the ground truth was defined by expert endoscopists. Figure 6 shows a set of representative images of normal TM. The results of segmentation algorithm are shown in Figures 6(a)–6(d). Figures 6(e)–6(h) indicate the comparison of the ground truth and segmentation results shown in pairs. We found that the result of segmentation of TM includes malleus in the red image which is better than the other images because it has the closest border with the doctor's result and the contour of the red image is smoother than the others. To demonstrate that results are reliable, the need for a method could accurately evaluate the segmentation results of TM. The suitable parameters are the DSC value and the maximum HD.

Firstly, the DSC could compute the ratio of overlap between the segmentation result by using algorithm and the ground truth defined by the endoscopy experts. However, the active contour algorithm based on different images gives completely different results in shape as well as boundary size with the same mask and number of loops. The eardrum segmentation results in white and green images (Figures 6(e) and 6(g)) are significantly different from ground truth, although the DSC index is quite high on four different wavelength images. The boundary in the white and green images has a part protruded and recessed in the pars flaccida leading to the fact that the border is not smoothed, while the DSC value computed based on the number of pixels coincided between the segmentation result and the ground truth. Thus, we require another standard parameter which could measure the coincidences of the segmentation results compared with the ground truth and the maximum HD (the Hausdorff distance) is one of the appropriate options.

The DSC (see Figure 7(a)) and the maximum HD (see Figure 7(b)) diagrams are the average value of the segmentation results in 12 series of images showing the difference of four different wavelengths. Generally, in the DSC chart, the red images group have the highest accurate average value of about 0.91 (higher DSC value is good). In contrast, in the maximum HD chart, the red images group have the lowest average value of about 9.00 in length unit (lower max HD value is good) that demonstrated the consistency of the TM segmentation results. The obtained results showed a good result when using active contour on red image to segment the TM which include malleus, with the highest DSC value and the lowest maximum HD value.

4. Conclusions

Endoscopy is a standard method for diagnosing ear disease, combined with a multispectral light source that can provide more information about the pathology and morphology of the middle ear. We modified the multispectral LED light source based on two maximum absorption peaks and one minimum absorption peak of the hemoglobin corresponding to the blue, green, and red spectrum. The study results indicated that the red illumination image not only fully described the contrast enhancement of the tympanic membrane and malleus compared to the surrounding tissue but also minimized the noise appearing on the image. We demonstrate the efficacy of this research in an TM segmentation application with high accuracy. Determining exactly the position as well as the boundary of TM helps to evaluate middle ear disease faster and better. Increasing the middle ear components contrast, especially the TM and malleus, does not only improve the ability to observe directly the morphological structure tympanic membrane in some cases of inflammation, redness, and vascular proliferation but also support the preprocessing step in biomedical image analysis researches.

Data Availability

In this study, 12 volunteers with 48 images of the tympanic membrane, accepted by the ethics committees of Vietnam National University, Ho Chi Minh City, Vietnam from 2019, were used as study objects. The authors cannot share it or make it available online for privacy reasons.

Conflicts of Interest

The authors declare that there are no conflicts of interest regarding the publication of this paper.

Acknowledgments

This research was funded by Ho Chi Minh City University of Technology–VNU-HCM, under grant number T-KHUD-2019-57.

References

[1] D. Kapsokalyvas, D. N. Bruscino, G. V. Cannarozzo et al., "Spectral morphological analysis of skin lesions with a polarization multispectral dermoscope," *Optics Express*, vol. 21, no. 4, pp. 4826–4840, 2013.

[2] J. Spigulis, A. I. Oshina, A. Berzina, and A. Bykov, "Smartphone snapshot mapping of skin chromophores under triple-wavelength laser illumination," *Journal of Biomedical Optics*, vol. 22, no. 9, p. 091508, 2017.

[3] L. Rey-Barroso, F. Burgos-Fernández, X. Delpueyo et al., "Visible and extended near-infrared multispectral imaging for skin cancer diagnosis," *Sensors*, vol. 18, no. 5, p. 1441, 2018.

[4] S. Ortega, H. Fabelo, D. K. Iakovidis, A. Koulaouzidis, and G. Callico, "Use of hyperspectral/multispectral imaging in gastroenterology. Shedding some–different–light into the dark," *Journal of Clinical Medicine*, vol. 8, no. 1, pp. 1–21, 2019.

[5] S.-J. Bae, D.-S. Lee, V. Berezin, U. Kang, and K.-H. Lee, "Multispectral autofluorescence imaging for detection of cervical lesions: a preclinical study," *Journal of Obstetrics and Gynaecology Research*, vol. 42, no. 12, pp. 1846–1853, 2016.

[6] T. A. Valdez, N. Spegazzini, R. Pandey et al., "Multi-color reflectance imaging of middle ear pathology in vivo," *Analytical and Bioanalytical Chemistry*, vol. 407, no. 12, pp. 3277–3283, 2015.

[7] J. A. Carr, T. A. Valdez, O. T. Bruns, and M. G. Bawendi, "Using the shortwave infrared to image middle ear pathologies," *Proceedings of the National Academy of Sciences*, vol. 113, no. 36, pp. 9989–9994, 2016.

[8] N. Bhetwal and J. R. McConaghy, "The evaluation and treatment of children with acute otitis media," *Primary Care: Clinics in Office Practice*, vol. 34, no. 1, pp. 59–70, 2007.

[9] M. M. Khan, R. F. Labadie, and J. H. Noble, "Preoperative prediction of angular insertion depth of lateral wall cochlear implant electrode arrays," *Journal of Medical Imaging*, vol. 7, no. 3, Article ID 031504, 2020.

[10] M. M. R. Khan, R. F. Labadie, and J. H. Noble, "Preoperative angular insertion depth prediction in case of lateral wall cochlear implant electrode arrays," in *Proceedings of the Medical Imaging 2020: Image-Guided Procedures, Robotic Interventions, and Modeling*, vol. 11315, p. 113151R International Society for Optics and Photonics, Houston, TX, USA,March 2020.

[11] X.-h. Xie, M. Mirmehdi, R. Maw, and A. Hal, "Detecting abnormalities in tympanic membrane images," in *Proceedings of the 9th Medical Image Undestanding and Analysis (MIUA)*, Medical Image Understanding an Analysis,Bristol, UK, 2005.

[12] A. Kuruvilla, N. Shaikh, A. Hoberman, and J. Kovačević, "Automated diagnosis of otitis media: vocabulary and grammar," *International Journal of Biomedical Imaging*, vol. 2013, pp. 1–15, Article ID 327515, 2013.

[13] A. Ferreira, F. Gentil, and J. M. R. S. Tavares, "Segmentation algorithms for ear image data towards biomechanical studies," *Computer Methods in Biomechanics and Biomedical Engineering*, vol. 17, no. 8, pp. 888–904, 2014.

[14] J. Seok, J.-J. Song, J.-W. Koo, K. H. Chan, and B. Y. Choi, "The semantic segmentation approach for normal andpathologic tympanic membrane using deep learning," *BioRxiv*, 2019.

[15] E. Başaran, Z. Cömert, and Y. Celik, "Convolutional neural network approach for automatic tympanic membrane detection and classification," *Biomedical Signal Processing and Control*, vol. 56, Article ID 101734, 2020.

[16] S. Lankton and A. Tannenbaum, "Localizing region-based active contours," *IEEE Transactions on Image Processing*, vol. 17, no. 11, pp. 2029–2039, 2008.

[17] K. H. Zou, S. K. Warfield, A. Bharatha et al., "Statistical validation of image segmentation quality based on a spatial overlap index," *Academic Radiology*, vol. 11, no. 2, pp. 178–189, 2004.

[18] D. P. Huttenlocher, G. A. Klanderman, and W. J. Rucklidge, "Comparing images using the Hausdorff distance," *IEEE Transactions on Pattern Analysis and Machine Intelligence*, vol. 15, no. 9, pp. 850–863, 1993.

[19] P. Taroni, A. M. Paganoni, F. Ieva et al., "Non-invasive optical estimate of tissue composition to differentiate malignant from benign breast lesions: a pilot study," *Scientific Reports*, vol. 7, no. 1, pp. 1–11, 2017.

[20] K. Stenfeldt, C. Johansson, and S. Hellström, "The collagen structure of the tympanic membrane," *Archives of Otolaryngology-Head & Neck Surgery*, vol. 132, no. 3, pp. 293–298, 2006.

[21] S. Danti, C. Mota, D. D'alessandro et al., "Tissue engineering of the tympanic membrane using electrospun PEOT/PBT copolymer scaffolds: a morphological in vitro study," *Hearing, Balance and Communication*, vol. 13, no. 4, pp. 133–147, 2015.

Hindawi
Journal of Healthcare Engineering
Volume 2020, Article ID 3743171, 14 pages
https://doi.org/10.1155/2020/3743171

Research Article

Classification of Alzheimer's Disease and Mild Cognitive Impairment Based on Cortical and Subcortical Features from MRI T1 Brain Images Utilizing Four Different Types of Datasets

Saidjalol Toshkhujaev,[1] Kun Ho Lee,[2,3] Kyu Yeong Choi,[2] Jang Jae Lee,[2] Goo-Rak Kwon,[1,2] Yubraj Gupta,[1,2] and Ramesh Kumar Lama[1,2]

[1]*School of Information Communication Engineering, Chosun University, 309 Pilmun-Daero, Dong-Gu, Gwangju 61452, Republic of Korea*
[2]*National Research Center for Dementia, Chosun University, 309 Pilmun-Daero, Dong-Gu, Gwangju 61452, Republic of Korea*
[3]*Department of Biomedical Science, College of Natural Sciences, Chosun University, 309 Pilmun-Daero, Dong-Gu, Gwangju 61452, Republic of Korea*

Correspondence should be addressed to Goo-Rak Kwon; grkwon@chosun.ac.kr

Received 9 November 2019; Revised 9 July 2020; Accepted 14 July 2020; Published 1 September 2020

Academic Editor: Belayat Hossain

Alzheimer's disease (AD) is one of the most common neurodegenerative illnesses (dementia) among the elderly. Recently, researchers have developed a new method for the instinctive analysis of AD based on machine learning and its subfield, deep learning. Recent state-of-the-art techniques consider multimodal diagnosis, which has been shown to achieve high accuracy compared to a unimodal prognosis. Furthermore, many studies have used structural magnetic resonance imaging (MRI) to measure brain volumes and the volume of subregions, as well as to search for diffuse changes in white/gray matter in the brain. In this study, T1-weighted structural MRI was used for the early classification of AD. MRI results in high-intensity visible features, making preprocessing and segmentation easy. To use this image modality, we acquired four types of datasets from each dataset's server. In this work, we downloaded 326 subjects from the National Research Center for Dementia homepage, 123 subjects from the Alzheimer's Disease Neuroimaging Initiative (ADNI) homepage, 121 subjects from the Alzheimer's Disease Repository Without Borders homepage, and 131 subjects from the National Alzheimer's Coordinating Center homepage. In our experiment, we used the multiatlas label propagation with expectation–maximization-based refinement segmentation method. We segmented the images into 138 anatomical morphometry images (in which 40 features belonged to subcortical volumes and the remaining 98 features belonged to cortical thickness). The entire dataset was split into a 70 : 30 (training and testing) ratio before classifying the data. A principal component analysis was used for dimensionality reduction. Then, the support vector machine radial basis function classifier was used for classification between two groups—AD versus health control (HC) and early mild cognitive impairment (MCI) (EMCI) versus late MCI (LMCI). The proposed method performed very well for all four types of dataset. For instance, for the AD versus HC group, the classifier achieved an area under curve (AUC) of more than 89% for each dataset. For the EMCI versus LMCI group, the classifier achieved an AUC of more than 80% for every dataset. Moreover, we also calculated Cohen kappa and Jaccard index statistical values for all datasets to evaluate the classification reliability. Finally, we compared our results with those of recently published state-of-the-art methods.

1. Introduction

The occurrence of the most serious and common neurodegenerative disease, Alzheimer's disease (AD), is dramatically increasing among the elderly. Among people of ages ranging from 60 to 84, 24.3 million are suffering from AD [1]. The early diagnosis of AD and the best prognosis of mild impairment are possible because of an increasing list of possible biomarkers (from genetics, cognition, proteomics, and neuroimaging) [2]. Mild cognitive impairment (MCI) is the level between the predictable cognitive deterioration of regular aging and the more serious decline of dementia. At the beginning of the MCI stage, there might be difficulties with thinking, language, and memory that are more than ordinary age-related changes. A reason for differentiating the above patients from those with prodromal AD at the MCI level is that intervention early in the course of the illness may help postpone the onset and reduce the risk of AD [3]. Such intervention later in the progression of the illness might limit the disease, but it might not be possible to shift the pathology-induced neurological damage after it has already occurred. Therefore, analysis and identification of presymptomatic AD at the MCI point are highly important. Such treatment will be much more central and compelling as improved treatment becomes available.

In neuroimaging, the main task is labeling anatomical structures in magnetic resonance imaging (MRI) brain scans with accuracy. For clinical decision-making, regional volume measurement is important, as well as accurate segmentation [4]. Currently, there is no treatment method for AD, but many drugs are under development, and it is predicted that a cure will be found soon. Therefore, neuroimaging makes an optimistic prognosis more likely, and assessments by structural MRI (sMRI) can be used to check medial temporal lobe (MTL) and positron emission tomography (PET) fluorodeoxyglucose (FDG) or amyloid results. Medial temporal lobe frameworks are essential for producing new memories and for the improvement of AD [5]. Medial temporal lobe atrophy (MTA) degeneration and the associated episodic memory impairment are label features of AD, and both impair over the method of illness [5, 6]. Moreover, MTA is determined by utilizing region of interest- (ROI-) based [7], voxel-based [8], and vertex-based [5] approaches. In this research, the focus is on binary arrangement among AD, health control (HC), early MCI (EMCI), and late MCI (LMCI) utilizing sMRI. According to the atrophy assessment from MRI scans, the level of neurodegeneration and intensity can be determined. Studies have used morphometric approaches, such as the volume of interest (VOI) and ROI voxels for automatic segmentation of sMRI images. The sMRI volume involves measurement of the medial progressive lobe and hippocampus [9]. Numerous machine-learning methods have been implemented to differentiate the binary classifications of AD, HC, and MCI due to AD (mAD) and asymptomatic AD (aAD). Only using unique modalities, such as the hippocampus or amyloid imaging biomarkers, could be less sensitive in analyzing AD progression, mostly at the symptomatic level. Currently, the relevance of biomarkers for neurodegeneration, which is an analytical component of AD pathophysiology in prodromal and early-stage dementia, is widely acknowledged [10]. The most-important biomarkers for early detection of AD are the volumetric measurement of cortical thickness and subcortical volume. Studying the cortical thickness is an extensively recognized method for investigating the size of gray matter atrophy and is at the cutting edge of AD research. Cortical thinning has been found in MCI and AD [11]. However, for subcortical neurofibrillary tangle and amyloid construction in AD, MRI investigation has recently drawn attention to AD-correlated subcortical complex changes. New segmentation methods can assess subcortical volumes and provide a basis for subcortical shape analysis [11]. Many classification algorithms and approaches are based on machine learning, such as support vector machine (SVM), k-nearest neighbor (KNN), random forest (RF), and other ensemble classifiers. Among these, the SVM algorithm is commonly utilized because of its good accuracy and sensitivity that can deal with high-dimensional data. The SVM classification method provides a first step for recognizing data from the training dataset included in well-characterized subjects with known states, for which labels are given for the subjects [12]. The margin of the training data is maximized by composing the optimal splitting hyperplane or regular hyperplanes in a solitary or higher-dimensional plane with proposed classifier. At the testing stage, a test dataset is based on the hyperplane learned in the classification [13]. It is common for T1-weighted MRI images of each subject to be separated automatically into ROIs according to three anatomical views (sagittal, coronal, and axial), as shown in Figure 1. They are used as features for classification.

Recently, Liu et al. [14] proposed deep learning based on multiclass classification among normal control (NC), MCI not converted (ncMCI), MCI transformers converted (cMCI), and AD patients grounded on 83 ROI of MRI images and the conforming disclosed PET images. Stacked autoencoders were utilized as unsupervised learning to gain high-level features, and softmax logistic regression was adopted as a classifier. Nozadi et al. [15] researched an approach for a pipeline utilizing learned features from semantically labeled PET images to show group classification. In that research, the ADNI dataset was used, and the results were validated. In classification, they used SVM classifier with radical basis function (RBF) kernel and random forest (RF) with FDG and AV-45 biomarkers of PET image modality for AD, NC, EMCI, and LMCI groups. The FDG-PET shows good accuracy such as 91.7% for AD versus NC with RBF-SVM classifier compared to AV-45-PET. Moreover, FDG-PET demonstrates better results for EMCI versus LMCI with RBF-SVM than AV-45-PET. Gupta et al. [16] proposed a machine-learning-based framework to distinguish subjects with AD from those with MCI by using four different biomarkers: sMRI, the apolipoprotein E (APOE) genotype, cerebrospinal fluid (CSF) protein level, and FDG-PET from the ADNI dataset. According to binary

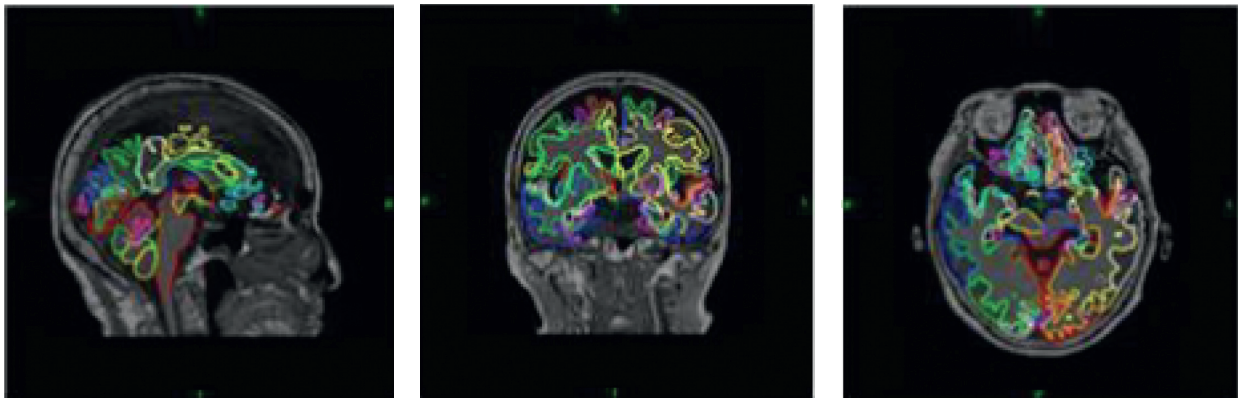

(a) (b) (c)

Figure 1: Cross-sectional segmentation results for T1-weighted MRI images: (a) axial, (b) coronal and sagittal, and (c) view planes.

classification, the combined method showed area under the receiver operating characteristic curves of 98.33%, 93.59%, 96.83%, 94.64%, 96.43, and 95.24% for AD versus HC, MCI stable (MCIs) versus cMCI, AD versus MCIs, AD versus cMCI, HC versus cMCI, and HC versus MCIs, respectively. Gorji and Naima [17] have employed a convolutional neural network (CNN) based deep learning approach for discriminating healthy people from patients with EMCI and LMCI. In their research, the ADNI dataset was used, and their proposed method has gained 94.54% accuracy, 91.70% sensitivity, and 97.96% specificity with the sagittal part of MRI for CN versus LMCI. Chyzhyk et al. [18] utilized lattice-independent component analysis to combine the kernel transformation of data with the feature section stage. The generalization of the dendritic computing classifiers was developed by that approach. For classification of NC versus AD patients, they also used the OASIS dataset and method with an accuracy of 74.75%, sensitivity of 96%, and specificity of 52.5%. Zang et al. [19] utilized operative feature consequent from functional brain network of three frequency bands during resting states for the efficiency of the classification context to classify subjects with EMCI versus LMCI. Their approached method demonstrates that the functional network features chosen by the minimal redundancy maximal relevance (mRMR) algorithm improve the distinguishing between EMCI versus LMCI compared with others chosen by stationary selection (SS-LR) and Fisher score (FS) algorithms. The chosen slow-5 band shows better accuracy compared with other bands such as 83.87% accuracy, 86.21% sensitivity, and 81.21% specification for EMCI versus LMCI. Cuingnet et al. [20] employed 10 approaches for clinically abnormal subject versus healthy groups by using an sMRI-based feature extraction technique. This approach included three methods based on cortical thickness, and five voxel-based and two other methods for the hippocampus. When the technique was used, AD versus HC achieved 81% sensitivity and 95% specificity; stable MCI and progressive MCI (P-MCI) had a sensitivity of 70% and specificity of 61%; and HC versus P-MCI had 73% and 85% sensitivity and specificity, respectively. Farhan et al. [21] utilized the right and left areas of the hippocampus, as well as the volume of gray matter, white matter, and CSF extracted from sMRI brain images. Then, four types of classification were evaluated to achieve good accuracy: SVM, multilayer perceptron, j48, and an ensemble classifier. The ensemble classifier had a high accuracy of 93.75%. Cho et al. [22] studied the incremental learning process based on the longitudinal frequency, which is represented by cortical thickness implemented on 131 ncMCI and 72 cMCI subjects. When the method was used for cMCI versus ncMCI, the sensitivity and specificity were 63% and 76%, respectively, which is a better result than that reported previously [21]. Wolz et al. [23] employed four kinds of automatic feature extraction methods (manifold-based learning, cortical thickness, tensor-based morphometry, and hippocampal volume) based on sMRI for 834 subjects from the ADNI dataset AD versus MCI and AD versus HC groups. The linear discriminant analysis (LDA) and SVM classification techniques were compared by manipulating MCI prediction and AD classification. In AD versus HC classification, LDA achieved 89% accuracy, and the sensitivity and specificity were 93% and 85%, respectively. Specifically, fusion features and the LDA classifier showed the best result for the classification of MCI-converted and MCI-stable subjects (68% accuracy, 67% sensitivity, and 69% specification). Recently, Gupta et al. [5] proposed four classifier methods—SVM, *k*-nearest neighbors, softmax, and naïve Bayes (NB)—for binary classification of AD versus HC, HC versus mAD, and mAD versus aAD and for tertiary classification of AD versus HC versus mAD and AD versus HC versus aAD utilizing subcortical and cortical features based on 326 subjects downloaded from the Gwangju Alzheimer's disease and Related Dementia (GARD) dataset website. The segmented dataset was parceled into a 70 : 30 ratio, and 70% was used as a training set. The remainder was used to obtain unbiased estimation performance as a test set. PCA was manipulated for dimensionality reduction purposes and obtained a 99.06% F1 score by the softmax classifier for AD versus HC binary classification. The SVM classifier achieved for HC versus mAD, AD versus aAD binary, and AD versus HC versus mAD tertiary classification F1 scores of 99.51%, 97.5%, and 99.99%, respectively. NB performed well for AD

versus HC versus aAD tertiary classification with an F1 score of 95.88%. Moreover, to confirm the efficiency of the model, the OASIS dataset was employed.

Compared to related early works, this research addresses improving the accuracy and constancy of binary classification by comparing it with three kinds of geographical sMRI dataset. Moreover, all related works used different types of automated feature extraction method and segmentation toolbox. This work focused on the best accurate and clear segmentation method, which is multiatlas label propagation (MALP) with expectation–maximization- (EM-) based refinement (MALPEM) [24]. The best classifier, RBF-SVM, was utilized with the proposed classifier method. The GARD dataset was employed to classify the AD versus NC and EMCI versus LMCI binary classifications based on subcortical volume and cortical thickness from the sMRI brain images. Finally, the segmented features were passed through the RBF-SVM classifier and compared to the other three sMRI datasets.

2. Materials and Methods

2.1. Subjects. The data used in this study were collected from the NRCD, National Alzheimer's Coordinating Center (NACC), Alzheimer's Disease Repository Without Borders (ARWIBO), and ADNI. All preprocessed brain images were selected. The GARD consists of 81 AD subjects (39 males, 42 females; age ± SD = 71.86 ± 7.09 years, education level = 7.34 ± 4.88, range = 0–18), 171 cognitively normal HC subjects (83 males, 88 females; age ± SD = 71.66 ± 5.43 years, education level = 9.16 ± 5.54, range = 0–22), 39 patients with mAD (25 males, 14 females; age ± SD = 73.23 ± 7.09 years, education level = 8.20 ± 5.19, range = 0–18), and 35 patients with aAD (15 males, 20 females; age ± SD = 72.74 ± 4.82 years, education level = 7.88 ± 6.30, range = 0–18). The NACC includes 26 AD subjects (11 males, 15 females; age ± SD = 73.33 ± 9.43 years, education level = 14.44 ± 3.58, range = 0–18), 42 cognitively normal HC subjects (22 males, 20 females; age ± SD = 65.98 ± 11.91 years, education level = 15.89 ± 2.96, range = 0–22), 30 patients with mAD (10 males, 20 females; age ± SD = 75.52 ± 8.62 years, education level = 14.91 ± 3.45, range = 0–18), and 33 patients with aAD (16 males, 17 females; age ± SD = 73.12 ± 8.92 years, education level = 14.39 ± 4.08, range = 0–18). The ARWIBO consists of 29 AD subjects (10 males, 19 females; age ± SD = 71.2 ± 4.14 years, education level = 8.37 ± 9.31, range = 0–18), 33 cognitively normal HC subjects (16 males, 17 females; age ± SD = 65.5 ± 9.09 years, education level = 10.0 ± 6.82, range = 0–22), 34 patients with mAD (14 males, 20 females; age ± SD = 69.7 ± 7.11 years, education level = 7.67 ± 4.21, range = 0–18), and 25 patients with aAD (10 males, 15 females; age ± SD = 69.45 ± 3.22 years, education level = 7.97 ± 5.21, range = 0–18). The ADNI consists of 32 AD subjects (17 males, 15 females; age ± SD = 72.14 ± 4.21 years, education level = 9.41 ± 3.78, range = 0–18), 28 cognitively normal HC subjects (18 males, 10 females; age ± SD = 64.02 ± 6.45 years, education level = 11.41 ± 6.56, range = 0–22), 25 patients with mAD (12 males, 13 females; age ± SD = 69.14 ± 8.35 years, education level = 7.99 ± 4.20, range = 0–18), and 38 patients with aAD (22 males, 16 females; age ± SD = 67.11 ± 5.81 years, education level = 8.02 ± 7.10, range = 0–18).

Tables 1–4 demonstrate the demographics of the 326 subjects from the GARD, 121 subjects from the ARWIBO, 131 subjects from the NACC, and 123 subjects from the ADNI for this study. The clinical variables and distinguishing statistics in demographics among the research groups were determined using the Welch independent samples *t*-test. In this research, the significance level was 0.05, which is a normal alpha value. In the GARD data case, the rate for females was greater than that of other groups except for the EMCI group. The levels of education were completely disparate in the pairwise comparisons among study groups. According to the comparison among the groups, the AD groups had the lowest level of education. In this study, to gain unbiased estimated performance, every dataset was randomly split into two parts with a 70 : 30 ratio for training and testing. The approach involved training with a training algorithm code. We tested the remaining dataset using the trained algorithm. Moreover, the analysis of the group performance was classified in terms of accuracy, specificity, sensitivity, precision, and F1 score utilizing a unique test set.

2.2. MRI Acquisition. A brain image occupies space in three-dimensional (3D) images, so we could use volume data to fill this space. The volume data are measured voxels, which look like the pixels utilized to display images only in 3D.

Standard 3T T1-weighted images were obtained utilizing the volumetric 3D MPRAGE protocol with a resolution $1 \times 1 \times 1$ mm (voxel size). All images were N4 bias corrected.

2.3. Feature Selection. Segmented MRI brain images have been used mostly for classification with machine learning and the subfield of machine-learning techniques. According to many types of studies, the subcortical part of the brain is easily affected by dementia and AD compared to the cortical part, but cortical thickness is an outstanding candidate for the treatment of AD. In this research, subcortical/cortical features were extracted by using MALPEM, and 138 features were achieved from 3D sMRI T1-weighted images. MALPEM is a collection of tools for distinguishing and visualization of cortical/subcortical parts of the brain based on the sagittal, axial, and coronal views in Figure 1. MALPEM was constructed using an automatic workflow consisting of several standard image-processing techniques, dividing 138 ROIs. In recent years, multiatlas segmentation has developed into one of the most accurate methods for the segmentation of T1-weighted images, mostly focusing on graph-cut or EM optimization. MALPEM [24] was evaluated as a top 3 method in a Grand Challenge on whole-brain segmentation at MICCAI 2012 (http://www.christianledig.com). The sMR images of all 701 subjects were segmented individually utilizing MALPEM as designated in previous research [3]. It consumed between 8 and 10 h for each subject. For this segmentation, the automatically explained

Table 1: Demographic characteristics of the studied population (from the GARD database).

Group	Subject number	Age	Gender		Education
			M	F	
AD	81	71.86 ± 7.09 [56–83]	39	42	7.34 ± 4.88 [0–18]
EMCI	39	73.23 ± 7.34 [49–87]	25	14	8.20 ± 5.19 [0–18]
LMCI	35	72.74 ± 4.82 [61–83]	15	20	7.88 ± 6.30 [0–18]
HC	171	71.66 ± 5.43 [60–85]	83	88	9.16 ± 5.54 [0–22]

Table 2: Demographic characteristics of studied population (from the ARWIBO dataset).

Group	Subject number	Age	Gender		Education
			M	F	
AD	29	71.24 ± 14.09 [59–80]	10	19	8.37 ± 3.78 [0–18]
EMCI	34	69.7 ± 7.11 [51–82]	14	20	7.67 ± 4.21 [0–18]
LMCI	25	69.45 ± 3.22 [59–79]	10	15	7.97 ± 5.21 [0–18]
HC	33	65.59 ± 9.12 [58–83]	16	17	10.06 ± 3.43 [0–22]

Table 3: Demographic characteristics of studied population (from the NACC dataset).

Group	Subject number	Age	Gender		Education
			M	F	
AD	26	73.33 ± 9.43 [50–78]	11	15	14.44 ± 3.58 [0–18]
EMCI	30	75.52 ± 8.62 [47–85]	10	20	14.91 ± 3.45 [0–18]
LMCI	33	73.12 ± 8.92 [58–80]	16	17	14.39 ± 4.08 [0–18]
HC	42	65.98 ± 11.91 [59–83]	22	20	15.89 ± 2.96 [0–22]

Table 4: Demographic characteristics of studied population (from the ADNI dataset).

Group	Subjects number	Age	Gender		Education
			M	F	
AD	32	72.14 ± 4.21 [54–79]	17	15	9.41 ± 3.78 [0–18]
EMCI	25	69.14 ± 8.35 [48–83]	12	13	7.99 ± 4.20 [0–18]
LMCI	38	67.11 ± 5.81 [60–81]	22	16	8.02 ± 7.10 [0–18]
HC	28	64.02 ± 6.45 [63–84]	18	10	11.41 ± 6.56 [0–22]

neuromorphometrics brain atlas ($n = 30$; provided by Neuromorphometrics, Inc., under academic subscription, http://Neuromorphometric/, last accessed 15 March 2018) was used. This atlas automatically distinguishes the whole-brain images into 40 noncortical and 98 cortical parts. MALP was utilized to acquire the specific probability of a brain atlas for sMRI brain images as K, which should be segmented [3]. This probability is integrated into the EM framework as a spatial anatomical task. n is indicated as a voxel of K by $j = 1, \ldots n$; therefore, the intensities of the voxel $Z_i \in D$; image should be described as $K = \{Z_1, Z_2 \ldots Z_n\}$. The probabilistic priors are produced through the transformation of manually generated L atlases into the coordinate space of the unseen image. For the propagation of the tag, the L transformations were measured using a nonrigid registering technique based on free-form deformation, which follows a previous rigid technique and some alignment. By using a locally weighted multiatlas fusion strategy, the probabilistic atlas was designed for image intensity normalization and rescaling by the Gaussian weighted sum of squared differentiation. The estimated hidden segmentation employing the observed intensities j followed the approach of Van Leemput et al. [25]. It was considered that the observed log-transformed intensities of the voxels refer to a spatial class N and are dispensed with mean φ_N and standard deviation ρ_N:

$$\psi = \{(\varphi_1, \rho_1), (\varphi_2, \rho_2), \ldots\ldots, (\varphi_N, \rho_N)\}. \quad (1)$$

The global Markov random fields approach was used for applying the regularization of the resulting segmentation. The EM algorithm makes segmentations with very low-intensity variance within the region (intraclass variance) compared to the "gold-standard" segmentations. Therefore, normalized intraclass variance was determined for each region ($\rho_{N\mathrm{Gold},k}$) by averaging the normalized standard deviations ($\rho N / \varphi N$) of every group over the training subjects. Moreover, the averaged (averaged over all training subjects segmented with a leave-one-out strategy) distributed standard deviation was measured within every region assembled by the EM algorithm ($\rho_{\mathrm{EM},k}$). By determining $\Delta_N = (p_{N\mathrm{Gold},k} - p_{\mathrm{EM},k})^2$, it was evaluated by which value the intraclass variance of the spatial group might be enhanced on average to match the gold-standard innates better [26]. The final segmentation was created by fusing the refined labels for this subset with the labels from the MALP

approach for enduring parts. After completion of segmentation, all the segmented data were normalized to zero mean and component variance for every feature, as demonstrated in Figure 2, utilizing the ordinary scalar function of the scikit-learn library. According to normalization, ξ is a given data matrix where the subjects are in rows, and the features of subjects are in columns. The elements of normalized matrix illustrate ξ (m, n), and the equation is given by

$$\xi_{\text{norm},(m,n)} = \frac{\xi_{(m,n)} - \text{mean}(\xi_n)}{\text{std}(\xi_n)}. \quad (2)$$

Then, for reduction of dimensionality, PCA was executed [27], with all features designed into a lower-dimensional space. PCA map features in a new N-dimensional subspace should be less than those in the initial L-dimensional space. The new N variance is the principal component, and every principal component eliminates the maximum variance that is accounted for in all accomplishing components. The principal components can be illustrated by the following equation:

$$\text{PC}_j = m_1 k_1 + m_2 k_2 + \cdots\cdots + m_z k_z, \quad (3)$$

where PC_j is a principal component in j, y_z is an original feature in z, and m_z is a numerical coefficient of y_z. The observed original features are greater than or equal to the number of principal components. The achieved principal components for AD versus HC are illustrated in Figure 3. The component number was regulated by controlling the features greater than 96%. The first principal component gained 96% among all the other 83 features received after passing all 138 features. Hence, the first component was utilized for the classification of EMCI versus LMCI as well.

2.4. Classification Method. Previously, the cortical and subcortical region features were extracted by using an automatic toolbox (MALP-EM) based on sMRI T1-weighted images. The feature vectors covering mean-centered voxel intensities were constructed by fusing all features. The classification method used here is designed to fuse two resources of features: subcortical volume and cortical thickness. The above features are utilized for a framework decision to distinguish AD from other subjects. Moreover, when comparing the classification for two-part brain images—cortical and subcortical—by RBF-SVM machine-learning classifiers, in some dataset cases, the cortical thickness was determined with good accuracy; in another case, the subcortical provided better results.

2.5. SVM. This machine-learning classifier is being used widely to investigate sMRI data [5, 12, 20]. RBF-SVM is suitable for binary classification for separable and non-separable data. In the past decade, it has been employed as the most popular machine-learning tool in neuroimaging and neuroscience. This approach depends on selecting a critical point for the classification work. Support vectors are elements that are distinguished into two groups. RBF-SVM is a supervised learning classification algorithm and determines the optimal hyperplane that discriminates both modules with an extreme margin from support vectors during the training phase. The estimated hyperplane determines the classifier for the testing of a new data point. In some cases, such as linear ones, SVM might not guarantee a good result, so linear SVM is expanded by utilizing a kernel trick. The central idea of kernel methods is that the input data are designed into a higher-dimensional plane employing linear and nonlinear functions for known kernels. SVM kernels exploit nonlinear and linear RBF. Moreover, the linear kernel is a superior case of RBF. The linear kernel with a penalty parameter $\hat{C}$ has the same presentation as the RBF kernel with the parameters (c, y). The RBF has two parameters, c and y, that are good for an assumed problem. The main goal of analyzing good (c, y) is to enable the classification method to predict testing data accurately.

3. Results and Discussion

3.1. Background. In this experiment, the proposed method utilized the RBF-SVM classification algorithm. Then, all extracted features were split into the cortical thickness and subcortical volume in the MALPEM toolbox to distinguish between the AD versus HC and EMCI versus LMCI groups. This classification was performed to recognize how well the approach performs on the sMRI 3D images. In the beginning stage, normalization was designed for every subject. Furthermore, the PCA reduction of dimensionality method was employed to select the optimal number of principal components for every binary classification. In a different binary classification group, different numbers of principal components were gained. Moreover, to confirm the robustness of the classification result, 10-fold stratified K-fold (SKF) cross-validation (CV) was utilized.

3.2. Evaluation. The set of subjects was randomly split into two groups in a 70 : 30 ratio for training and testing to obtain unbiased estimates of the performance. The training set was used for analyzing the optimal hyperparameters of every technique and classifier. Furthermore, the testing set was utilized for classification achievement. For optimal hyperparameter estimation, SKF-CV was used based on the training set. Following the LIBSVM library, the linear SVM $\hat{C}$ kernel value and c, y parameters of the kernel were regulated. While choosing the default parameter features, SVM performed poorly on the preliminary data. Hence, to regulate the optimal parameters for c and y, the grid search method was used before c and y were utilized for training. For c and y, CV accuracy was selected as the best parameter. In this work, two parameters were set—$c = 1$ to 10 and $y = (1e^{-4}, 1e^{-2}, 0.0001)$—for every classification group. Then, to analyze the classifier for the training groups, the obtained optimized values were regulated. The assessment of binary classifiers was determined by using confusion metrics, which is a precise test covering binary classification tasks. The

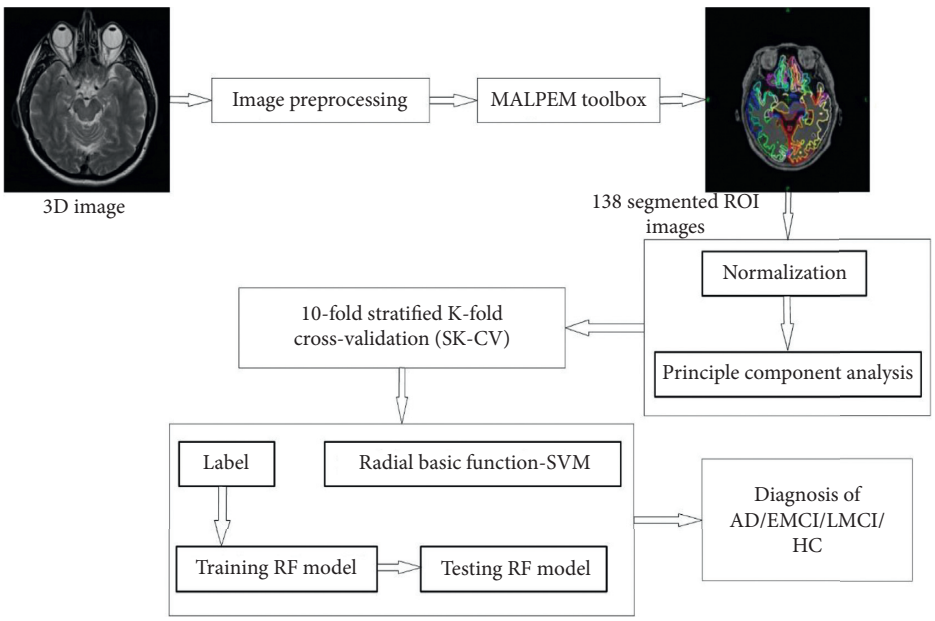

Figure 2: Proposed technique workflow.

diagonal elements of the metric demonstrate the corrected predictions created by the classifier. Then, elements could be split into two groups that express the controls of correctly identified true positive (TP) and true negative (TN). However, the subjects classified incorrectly can be defined as false positive (FP) and false negative (FN). The determination of accuracy in equation (4) is the number of samples in which the classifiers regulated correctly.

$$\mathrm{Acc} = \frac{\mathrm{TP} + \mathrm{TN}}{\mathrm{TP} + \mathrm{TN} + \mathrm{FP} + \mathrm{FN}}. \tag{4}$$

Moreover, considering only accurate measurement was not sufficient for the unstable class dataset and resulted in misleading estimation. Hence, the additional four assessment metrics should be adjusted: sensitivity, specificity, precision, and F1 score. They are designated as follows:

$$\mathrm{Sen} = \frac{\mathrm{TP}}{\mathrm{TP} + \mathrm{FN}}, \tag{5}$$

$$\mathrm{Spec} = \frac{\mathrm{TN}}{\mathrm{TN} + \mathrm{FP}}, \tag{6}$$

$$\mathrm{Ppv} = \frac{\mathrm{TP}}{\mathrm{TP} + \mathrm{FP}}. \tag{7}$$

$$\text{F1 score} = \frac{2\mathrm{TP}}{2\mathrm{TP} + \mathrm{FP} + \mathrm{FN}}. \tag{8}$$

Sensitivity, given in equation (5), illustrates the accuracy of the predicted group. Specificity, given in equation (6), illustrates the accuracy of the predicted absence group. Sensitivity, which is also called "recall" or "probability of detection," is the proportion of actual positives that are correctly determined. Similarly, specificity investigates the proportion of actual negatives that is not included in the class. Precision, given in equation (7) (positive predictive value), is the element of appropriate incidences between the repossessed incidences. F1 score, given in equation (8), determines the accuracy of a test. To assess that each method performs significantly better than a random classifier, the Cohen kappa and Jaccard distance were utilized. Cohen kappa determination is usually utilized to analyze interrater reliability. Rater reliability demonstrates the degree to which the data represented in the research are appropriate illustrations of the variables evaluated. The Cohen [28] is a statistic helpful for an interrater accuracy testing. The determination of the Cohen kappa can be executed based on the following equation:

$$\mathrm{k} = \frac{\Pr(a) - \Pr(e)}{1 - \Pr(e)}. \tag{9}$$

Here, P_r (a) demonstrates the observed agreement and P_r (e) illustrates chance agreement. The kappa can range between -1 and $+1$, and the kappa result is explained as follows: if the values are ≤ 0, there is no agreement; between 0.01 and 0.20, there is minor arrangement; between 0.21 and 0.40, there is known fair agreement; between 0.41 and 0.60, there is moderate agreement, between 0.61 and 0.80, there is substantial agreement; and from 0.81 to 1.00, there is nearly perfect agreement [29]. The Jaccard index determines how close the commonality of the two datasets can be a measured [30]. The Jaccard coefficient is given in the following equation:

$$J(M, N) = \frac{|M \cap N|}{|M \cup N|}. \tag{10}$$

The Jaccard index is a statistic utilized for measuring the diversity and similarity of sample sets.

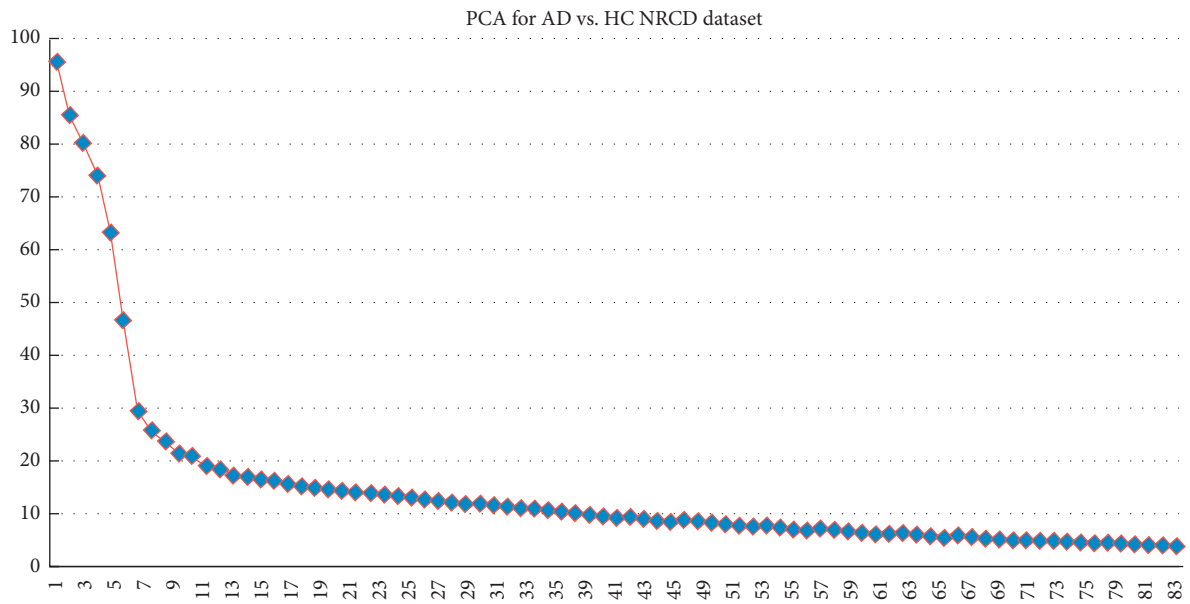

Figure 3: Number of principal components for AD versus HC.

The range of Jaccard coefficient measures from 0% to 100% is as follows:

Jaccard index = (the amount in equal sets)/(the amount in either set) × 100.

The process of calculating the Jaccard index is as follows: (1) calculate the number of both members that are proportional for both sets, (2) calculate the entire number of members (proportional and nonproportional), and split the number of common members (1) by the entire number of members (2), and (3) multiply by 100 [31].

3.3. Classification Results. The binary classification was utilized to analyze subcortical volume and cortical thickness volume of AD versus HC and EMCI versus LMCI subject groups. The results of classification are demonstrated in Table 5, and all results are illustrated in Figures 4(a) and 4(b). Kappa and Jaccard are shown in Figures 4(c) and 4(d). All processes were performed in a 64-bit Python 3.6 environment on Intel Core i7-8700 at 3.20 Hz and 16 GB of RAM running Ubuntu 16.04.

3.3.1. Binary Classification: AD versus HC and EMCI versus LMCI. According to the four datasets, two binary groups—AD versus HC and EMCI versus LMCI—were classified with subcortical volume and cortical thickness features by utilizing the RBF-SVM classification algorithm, and the result is illustrated in Table 5.

(1). AD versus HC. The result of classification for AD versus HC is given in Table 5 and Figures 4(a) and 4(c). In every classification situation, the database was divided into two separations in a 70 : 30 ratio. Each dataset shows better results for kappa and Jaccard statistics in the RBF-SVM classification technique. In the kappa statistics case, the GARD dataset cortical thickness feature gives the highest interrater reliability of 0.9342, and the ARWIBO dataset subcortical volume feature has 0.8939. In the Jaccard statistics case, the GARD dataset cortical thickness is 0.9091, the highest, and the ARWIBO dataset subcortical volume feature is 0.8889. Moreover, the GARD cortical thickness has a good F1 score, precision, specificity, and sensitivity (98.18%, 96.87%, 95.24%, and 98.18%, respectively).

(2). EMCI versus LMCI. The classification performance for EMCI versus LMCI is shown in Table 5 and Figures 4(b) and 4(d). Similarly, the kappa statistics for the GARD dataset subcortical volume feature shows the highest result—0.9043—and the ARWIBO dataset cortical feature is 0.8979. The Jaccard statistic for the GARD dataset subcortical volume feature had the highest result—0.9186. The NACC dataset subcortical volume feature is 0.9167. Furthermore, the GARD dataset subcortical volume feature has better results, with an F1 score, precision, specificity, and sensitivity of 96.45%, 100%, 100%, and 92.75%, respectively, compared to the cortical thickness.

3.3.2. Comparison with Related Recently Published Methods. As mentioned above, in the proposed method, four datasets were used: GARD, NACC, ARWIBO, and ADNI. Except for the GARD dataset, all are available for the public, and anyone can download them. The websites available are NACC (https://www.alz.washington.edu/), ARWIBO (https://www.gaaindata.org/partner/ARWIBO), and ADNI (http://adni.loni.usc.edu/).

There are 701 subjects: 326 (GARD), 131 (NACC), 121 (ARWIBO), and 123 (ADNI). The ages of all subjects are more than 47, and converting of mild cognitive stage to AD between 0 and 18 months. For segmentation, the T1-weighted sMRI imaging modality was utilized from each dataset. Moreover, the results of the proposed method were compared to recently published results, as shown in Tables 6 and 7.

Table 5: Result of four datasets for the subcortical and cortical parts for AD versus HC and EMCI versus LMCI.

AD vs. HC	Classifier	AUC	ACC	SEN	SPEC	PRE	F1	Kappa	Jaccard
ADNI cortical	SVM-RBF	91.67	91.57	81.82	100	100	90	0.8108	0.8333
ADNI subcortical		90.45	90.48	90.91	90	90.91	90.91	0.8091	0.8182
ARWIBO cortical		89.44	89.47	90	88.89	90	90	0.7889	0.8
ARWIBO subcortical		95.45	94.74	100	88.89	90.91	95.24	0.8939	0.8889
NRCD cortical		97.5	97.37	98.18	95.24	96.87	98.18	0.9342	0.9091
NRCD subcortical		95.71	93.42	96.3	86.36	94.55	95.41	0.8379	0.7917
NACC cortical		96.88	95.24	100	83.33	93.75	96.77	0.8772	0.8333
NACC subcortical		92.86	94.56	93.33	100	100	96.55	0.8889	0.8571
EMCI vs. LMCI	Classifier	AUC	ACC	SEN	SPEC	PRE	F1	Kappa	Jaccard
ADNI cortical	SVM-RBF	81.75	81.25	75	87.5	85.71	80	0.725	0.7158
ADNI subcortical		88.89	87.5	77.78	100	100	87.5	0.7538	0.7778
ARWIBO cortical		94.44	93.24	90	100	95.66	94.74	0.8979	0.8889
ARWIBO subcortical		95	94.87	88.89	92.75	100	94.12	0.8889	0.9012
NRCD cortical		92.86	90.91	91.45	100	100	88.89	0.8136	0.8271
NRCD subcortical		96.43	95.45	92.75	100	100	96.45	0.9043	0.9186
NACC cortical		91.67	89.47	87.78	89.57	90.24	87.5	0.7989	0.8133
NACC subcortical		95.83	94.74	92.56	100	100	93.33	0.8902	0.9167

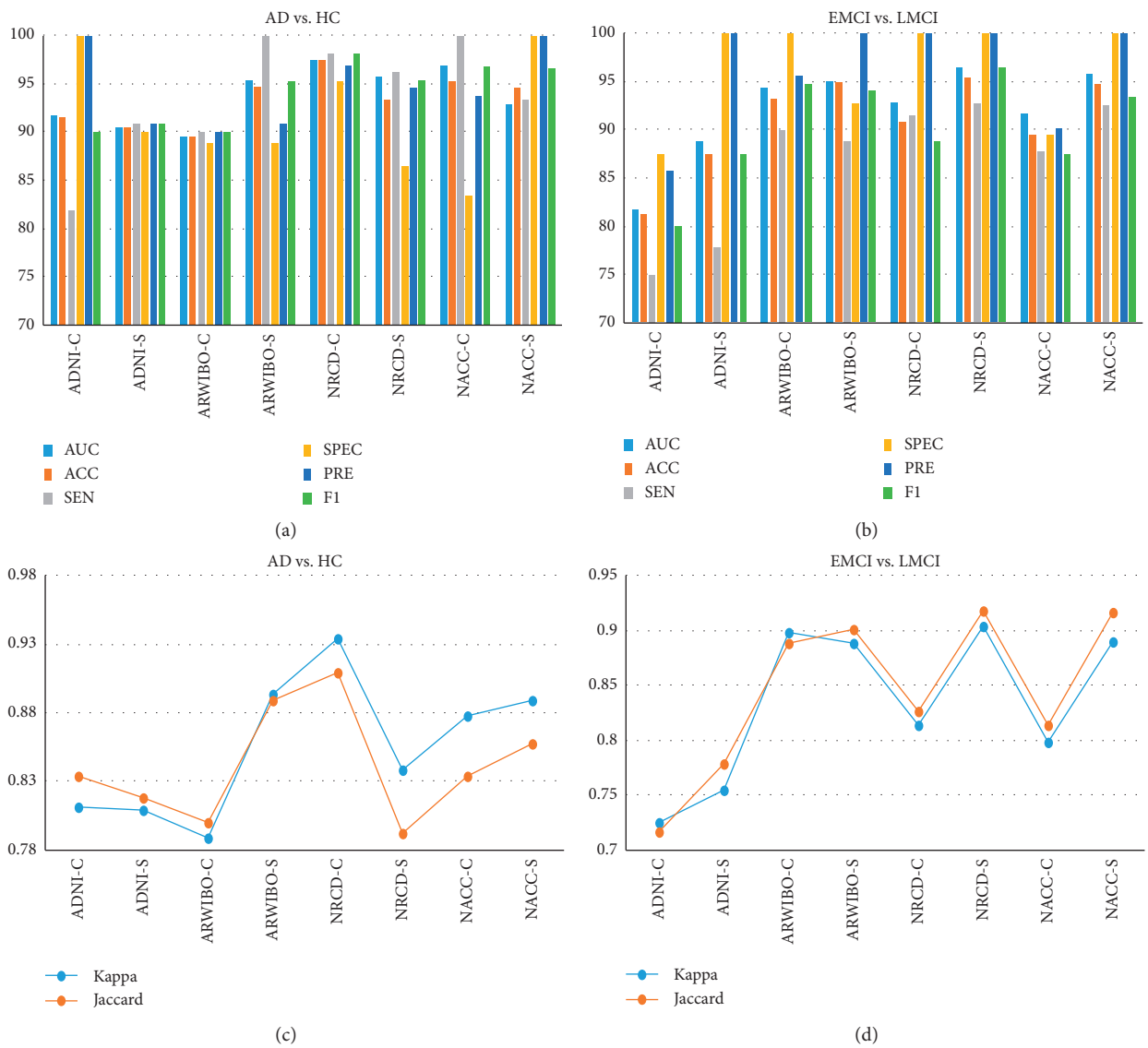

Figure 4: Classification reports of four datasets—ADNI-C (cortical), ADNI-S (subcortical), ARWIBO-C (cortical), ARWIBO-S (subcortical), NRCD-C (cortical), NRCD-S (subcortical), NACC-C (cortical), and NACC-S (subcortical)—with measurement performance (AUC, accuracy, sensitivity, specificity, precision, and F1 score): (a) AD versus HC, (b) EMCI versus LMCI, classification reports of four datasets with measurements of kappa and Jaccard, (c) AD versus HC, and (d) EMCI versus LMCI.

Table 6: Comparison of recently published works.

AD vs. HC						
Years	Approach	Dataset	ACC	SEN	SPEC	Classifier
2017	Tripathi et al. [13]	ADNI	85.98	75.55	90.30	RBF-SVM
2018	Nozadi and Kadoury [15]	ADNI	89.3	88.8	85.9	RBF-SVM
2018	Gupta et al. [5]	NRCD	99.34	98.14	100	Softmax
		OASIS	98.40	93.75	100	
2019	Proposed method	NRCD	**97.37**	**98.18**	**95.24**	RBF-SVM
		NACC	95.24	100	83.33	
		ARWIBO	94.74	100	88.89	
		ADNI	91.57	81.82	100	

Table 7: Comparison of recently published works.

EMCI vs. LMCI						
Years	Approach	Dataset	ACC	SEN	SPEC	Classifier
2017	Tripathi et al. [13]	ADNI	70.29	73.95	66.01	RBF-SVM
2018	Nozadi and Kadoury [15]	ADNI	67.6	70.1	70.7	RBF-SVM
2018	Gupta et al. [5]	NRCD	95.55	100	90.9	Softmax
2019	Zhang et al. [19]	ADNI	83.87	86.21	81.82	RBF-SVM
2019	Gorji and Naima [17]	ADNI	93.00	91.48	94.82	CNN
2019	Proposed method	NRCD	**95.45**	**92.75**	**100**	RBF-SVM
		NACC	94.74	92.56	100	
		ARWIBO	94.87	88.89	92.75	
		ADNI	87.50	77.78	100	

Tripathi et al. [13] proposed a method that used the RBF and linear SVM classifier for the automated pipeline which distinguishes subjects between AD, LMCI, EMCI, and HC with subcortical and hippocampal features gained from spherical harmonics (SPHARM-PDM) process by utilizing the ADNI dataset. The combination of voxel and SPHARM features shows 88.75% accuracy, 83.10% sensitivity, and 91.58% specificity for an AD versus HC group with a linear kernel SVM, whereas, for EMCI versus LMCI group, the same combined features show 70.95% accuracy, 75.56% sensitivity, and 65.47% specificity with linear SVM. Likewise, another study by Zhang et al. [19] used an SVM with nested cross-validation to distinguish the features into two groups to gain balanced results. The slow-5 frequency band shows 83.87% accuracy, 86.21% sensitivity, and 81.82% specificity for EMCI versus LMCI cohort by using the ADNI dataset. Gorji and Naima [17] have utilized CNN deep learning algorithms in their pipeline and utilizing it they have obtained a 93% accuracy, 91.48% sensitivity, and 94.82% specificity for EMCI versus LMCI using sagittal features from an MRI image. Furthermore, Nozadi and Kadoury [15] compared the FDG and AV-45 biomarkers of PET image and then employed RBF-SVM and RF for distinguishing AD, NC, EMCI, and LMCI with six groups by using ADNI dataset. Their approach showed accuracies of 91.7% and 91.2% for AD versus NC, each of RBF-SVM and RF with FDG-PET image modality. On the other hand, AV45 illustrates accuracies of 90.8% and 87.9% for AD versus NC with RBF-SVM and RF. For EMCI versus LMCI, FDG-PET provides better 53.9%, 64.1% accuracies compared with AV45 results in RBF-SVM and RF classifier. Gupta et al. [5] proposed a method utilizing the GARD dataset as a known private dataset, and the OASIS dataset was used for comparison. The four classifiers were utilized for binary and tertiary classification and achieved better results according to the classifier. For AD versus HC, the softmax classifier showed the highest accuracy of 99.34%, 100% specificity, and a precision of 100%. For the HC versus mAD case, the SVM classifier had an accuracy of 99.2% and a specificity and precision of 100%. The mAD versus aAD SVM provided good results as well, such as a 97.77% accuracy, 100% sensitivity, and 97.95% F1 score. In tertiary classification, SVM had the best accuracy of 99.42%, 99.18% sensitivity, and 99.99% precision in AD versus HC versus mAD. In AD versus HC versus aAD, the NB classifier had 96.53% accuracy, 95.88% sensitivity, and 97.64% specificity.

4. Discussion

In this research, the RBF-SVM method was employed for classification of subjects with AD versus HC and EMCI versus LMCI based on anatomical T1-weighted sMRI. The proposed method is shown in Figure 3. The subjects were divided into a ratio of 70 : 30 for training and testing purposes before being passed to the classifier. Then, the dimensionality reduction method was utilized by using the PCA function from the scikit-learn library. Subsequently, for the SVM classifier, the optimal structure value was regulated by employing SKF-CV and a grid search. Then, the above features were utilized to instruct the SVM classifier using the training dataset, and the testing dataset was assessed using the training method to determine the performance. The proposed method shows more than 90% accuracy for all datasets based on cortical

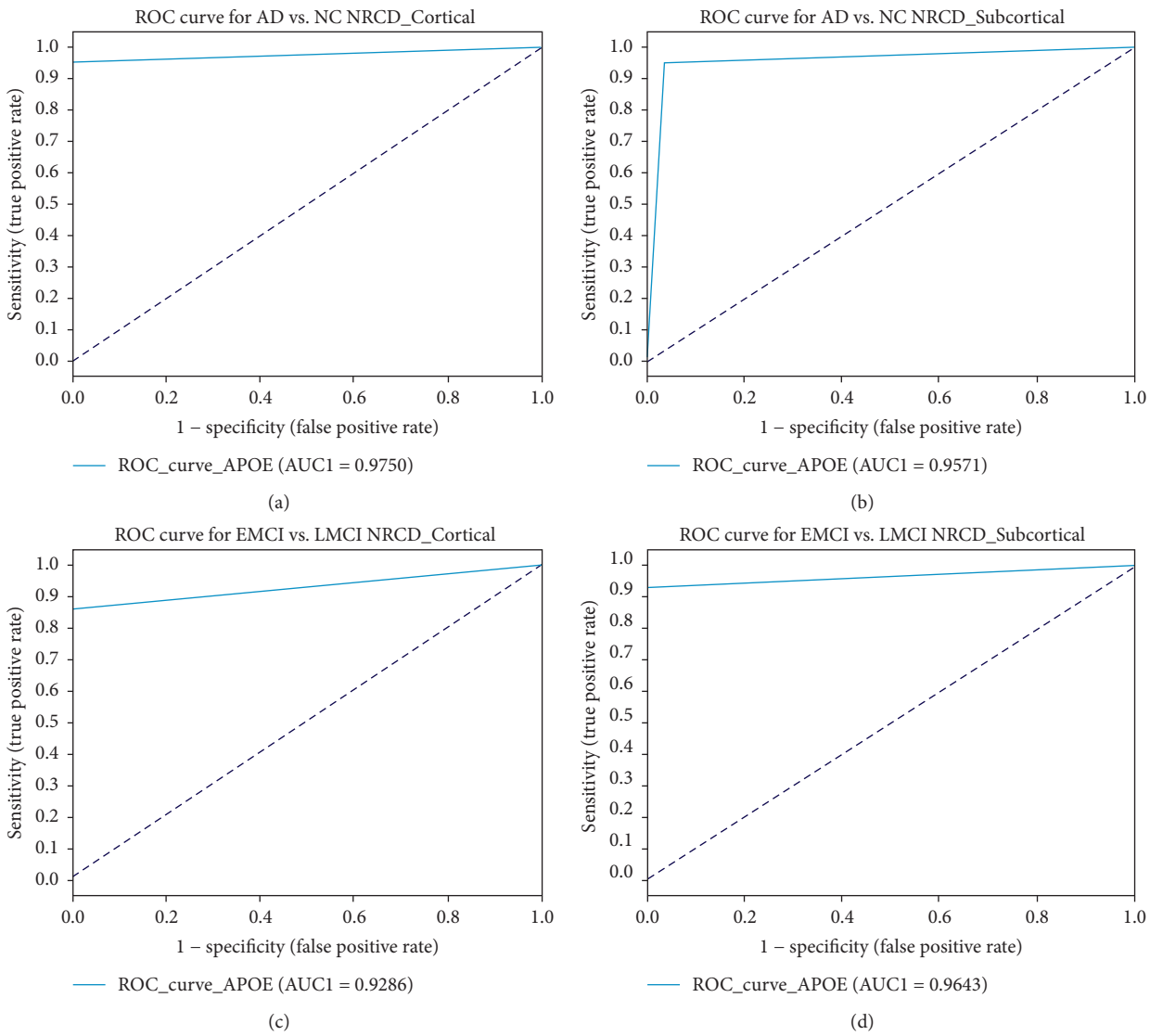

Figure 5: AUC-ROC performance for the GARD dataset: (a) AD versus HC cortical thickness, (b) AD versus HC subcortical, (c) EMCI versus LMCI cortical, and (d) EMCI versus LMCI subcortical.

and subcortical features in the AD versus HC groups. In the GARD dataset case, cortical thickness had the best accuracy, 97.37%, a sensitivity of 98.18%, and an F1 score of 98.18%. Moreover, kappa and Jaccard statistical analyses resulted in more than 0.80 for all datasets in AD versus HC binary classification.

In the EMCI versus LMCI group, GARD subcortical volumes had the highest accuracy among all datasets—95.45% accuracy, 100% precision, and 100% specificity. The Cohen kappa and Jaccard statistical volume produced good results as well. Moreover, GARD had a good AUC for the subcortical volume and cortical thickness of both groups, as given in Figure 5. In the ADNI dataset case (AD versus HC), the cortical thickness showed 100% specificity, 100% precision, and an accuracy of 91.57%. The EMCI versus LMCI subcortical volume had a specificity and precision of 100%. In the ARWIBO dataset case (AD versus HC), the subcortical volume had 100% sensitivity, 94.74% accuracy, and 95.24% F1 score, but for EMCI versus LMCI, the cortical thickness had a specificity of 100%, precision of 95.66%, and 94.74% F1 score. Furthermore, in the NACC dataset case (AD versus HC), the subcortical volume was 100%, with 100% specificity and precision and a 96.55% F1 score. Likewise, the EMCI versus LMCI subcortical volume had a specificity and precision of 100% and an accuracy of 94.74%. In both binary classifications, the proposed method obtained good results compared to those proposed in other works. In addition, the Cohen kappa and Jaccard results demonstrate excellent statistical analysis for ADNI, GARD, ARWIBO, and NACC.

5. Conclusions

A novel method for automatic classification, AD from MCI (early or late converted to AD) and an HC, was developed by utilizing the features of cortical thickness and subcortical

volumes. The features were extracted from a MALPEM toolbox, and classification was performed by the RBF-SVM classifier based on the GARD dataset. They were compared to three datasets. The results of this research prove that the proposed approach is efficient for future clinical prediction between the subcortical view of EMCI versus LMCI and the cortical view of AD versus HC, which are shown in Table 5. Based on the subcortical volume and cortical thickness, the proposed method obtained different accuracies according to the different databases, such as the GARD and NACC dataset AD versus HC group cortical thickness accuracies of 97.37% and 95.24%. The subcortical volumes of ARWIBO and NACC for the AD versus HC group were 94.74% and 94.56%.

In this research, only the subcortical volume and cortical thickness features were considered for the classification procedure. In the future, it is planned to examine classifier multimodality features of the brain biomarkers and non-imaging biomarkers for diagnosis of AD. Furthermore, we are planning a future work to compare state-of-the-art and recently published methods with different available datasets for early prediction of AD.

Data Availability

The Gwangju Alzheimer's disease and Related Dementia (GARD) dataset was used to support the findings of this study. The GARD is a private dataset that was generated in Chosun University hospitals, and it belongs to Chosun University. The authors cannot share it or make it available online for privacy reasons. Moreover, to compare the proposed approach with other datasets, the authors downloaded the NACC dataset from https://www.alz.washington.edu, the ARWIBO one from https://www.gaaindata.org, and the ADNI one from http://adni.loni.usc.edu.

Conflicts of Interest

The authors declare that there are no conflicts of interest regarding the publication of this paper.

Authors' Contributions

Saidjalol Toshkhujaev and Kun Ho Lee contributed equally to this work.

Acknowledgments

This work was supported by the National Research Foundation of Korea (NRF) grant funded by the Korea government (MSIT) (nos. NRF-2019R1A4A1029769 and NRF-2019R1F1A1060166), and this research was supported by KBRI basic research program through Korea Brain Research Institute funded by Ministry of Science and ICT (20-BR-03-02). Data collection and sharing for this project was funded by the Alzheimer's Disease Neuroimaging Initiative (ADNI) (National Institutes of Health Grant U01 AG024904) and DOD ADNI (Department of Defense Award No. W81XWH-12-2–0012). As such, the investigators within the ADNI contributed to the design and implementation of ADNI and/or provided data but did not participate in analysis or writing of this report. A complete listing of ADNI investigators can be found at http://adni.loni.usc.edu/wp-content/uploads/how_to_apply/ADNI_Acknowledgment_List.pdf. ADNI is funded by the National Institute on Aging, the National Institute of Biomedical Imaging and Bioengineering, and through generous contributions from the following: AbbVie, Alzheimer's Association; Alzheimer's Drug Discovery Foundation; Araclon Biotech; BioClinica, Inc.; Biogen; Bristol-Myers Squibb Company; CereSpir, Inc.; Cogstate; Eisai Inc.; Elan Pharmaceuticals, Inc.; Eli Lilly and Company; EuroImmun; F. Hoffmann-La Roche Ltd and its affiliated company Genentech, Inc.; Fujirebio; GE Healthcare; IXICO Ltd.; Janssen Alzheimer Immunotherapy Research & Development, LLC.; Johnson & Johnson Pharmaceutical Research & Development LLC.; Lumosity; Lundbeck; Merck & Co., Inc.; Meso Scale Diagnostics, LLC.; NeuroRx Research; Neurotrack Technologies; Novartis Pharmaceuticals Corporation; Pfizer Inc.; Piramal Imaging; Servier; Takeda Pharmaceutical Company; and Transition Therapeutics. The Canadian Institutes of Health Research is providing funds to support ADNI clinical sites in Canada. Private sector contributions are facilitated by the Foundation for the National Institutes of Health (http://www.fnih.org). The grantee organization is the Northern California Institute for Research and Education, and the study is coordinated by the Alzheimer's Therapeutic Research Institute at the University of Southern California. ADNI data are disseminated by the Laboratory for Neuroimaging at the University of Southern California. Data used in preparation of this article were obtained from the National Alzheimer's coordination center (NACC) database, funded by NIA/NIH Grant U01 AG016976. NACC data are contributed by the NIA funded ADCs: P30 AG019610 (PI Eric Reiman, MD), P30 AG013846 (PI Neil Kowall, MD), P50 AG008702 (PI Scott Small, MD), P50 AG025688 (PI Allan Levey, MD, PhD), P50 AG047266 (PI Todd Golde, MD, PhD), P30 AG010133 (PI Andrew Saykin, PsyD), P50 AG005146 (PI Marilyn Albert, PhD), P50 AG005134 (PI Bradley Hyman, MD, PhD), P50 AG016574 (PI Ronald Petersen, MD, PhD), P50 AG005138 (PI Mary Sano, PhD), P30 AG008051 (PI Thomas Wisniewski, MD), P30 AG013854 (PI Robert Vassar, PhD), P30 AG008017 (PI Jeffrey Kaye, MD), P30 AG010161 (PI David Bennett, MD), P50 AG047366 (PI Victor Henderson, MD, MS), P30 AG010129 (PI Charles DeCarli, MD), P50 AG016573 (PI Frank LaFerla, PhD), P50 AG005131 (PI James Brewer, MD, PhD), P50 AG023501 (PI Bruce Miller, MD), P30 AG035982 (PI Russell Swerdlow, MD), P30 AG028383 (PI Linda Van Eldik, PhD), P30 AG053760 (PI Henry Paulson, MD, PhD), P30 AG010124 (PI John Trojanowski, MD, PhD), P50 AG005133 (PI Oscar Lopez, MD), P50 AG005142 (PI Helena Chui, MD), P30 AG012300 (PI Roger Rosenberg, MD), P30 AG049638 (PI Suzanne Craft, PhD), P50 AG005136 (PI Thomas Grabowski, MD), P50 AG033514 (PI Sanjay Asthana, MD, FRCP), P50 AG005681 (PI John Morris, MD), and P50 AG047270 (PI Stephen Strittmatter, MD, PhD). ARWiBo data (http://www.arwibo.it) was obtained from NeuGRID4You initiative funded by the

European Commission (FP7/2007–2013) under grant agreement no. 283562. The overall goal of ARWiBo is to contribute, thorough synergy with neuGRID (https://neugrid2.eu), to global data sharing and analysis in order to develop effective therapies, prevention methods, and a cure for Alzheimer' and other neurodegenerative diseases.

References

[1] C. P. Ferri et al., "Global prevalence of dementia: a Delphi consensus study," *The Lancet*, vol. 366, no. 9503, pp. 2112–2117, 2005.

[2] B. C. Riedel, M. Daianu, G. Ver Steeg et al., "Uncovering biologically coherent peripheral signatures of health and risk for Alzheimer's disease in the aging brain," *Frontiers in Aging Neuroscience*, vol. 10, p. 390, 2018.

[3] P. B. Rosenberg and C. Lyketsos, "Mild cognitive impairment: searching for the prodrome of Alzheimer's disease," *World Psychiatry*, vol. 7, no. 2, pp. 72–78, 2008.

[4] C. Ledig et al., "Multi-class brain segmentation using atlas propagation and EM-based refinement," in *Proceedings of the 2012 9th IEEE International Symposium On Biomedical Imaging (ISBI)*, pp. 896–899, Barcelona, Spain, May 2012.

[5] Y. Gupta, K. H. Lee, K. Y. Choi, J. J. Lee, B. C. Kim, and G.-R. Kwon, "Alzheimer's disease diagnosis based on cortical and subcortical features," *Journal of Healthcare Engineering*, vol. 2019, Article ID 2492719, 13 pages, 2019.

[6] Y. Gupta, K. H. Lee, K. Y. Choi, J. J. Lee, B. C. Kim, and G. R. Kwon, "Early diagnosis of Alzheimer's disease using combined features from voxel-based morphometry and cortical, subcortical, and hippocampus regions of MRI T1 brain images," *PLoS One*, vol. 14, no. 10, Article ID e0222446, 2019.

[7] K. R. Gray, R. Wolz, R. A. Heckemann, P. Aljabar, A. Hammers, and D. Rueckert, "Multi-region analysis of longitudinal FDG-PET for the classification of Alzheimer's disease," *NeuroImage*, vol. 60, no. 1, pp. 221–229, 2012.

[8] H. Hanyu, T. Sato, K. Hirao, H. Kanetaka, T. Iwamoto, and K. Koizumi, "The progression of cognitive deterioration and regional cerebral blood flow patterns in Alzheimer's disease: a longitudinal SPECT study," *Journal of the Neurological Sciences*, vol. 290, no. 1-2, pp. 96–101, 2010.

[9] J. Barnes, J. W. Bartlett, L. A. van de Pol et al., "A meta-analysis of hippocampal atrophy rates in Alzheimer's disease," *Neurobiology of Aging*, vol. 30, no. 11, pp. 1711–1723, 2009.

[10] C. R. Jack, D. A. Bennett, K. Blennow et al., "NIA-AA Research Framework: toward a biological definition of Alzheimer's disease," *Alzheimer's & Dementia*, vol. 14, no. 4, pp. 535–562, 2018.

[11] E. Braak and H. Braak, "Alzheimer's disease: transiently developing dendritic changes in pyramidal cells of sector CA1 of the Ammon's horn," *Acta Neuropathologica*, vol. 93, no. 4, pp. 323–325, 1997.

[12] B. Magnin, L. Mesrob, S. Kinkingnéhun et al., "Support vector machine-based classification of Alzheimer's disease from whole-brain anatomical MRI," *Neuroradiology*, vol. 51, no. 2, pp. 73–83, 2009.

[13] S. Tripathi, S. H. Nozadi, M. Shakeri, and S. Kadoury, ""Subcortical shape morphology and voxel-based features for Alzheimer's disease classification," in *Proceedings of the 2017 IEEE 14th International Symposium on Biomedical Imaging (ISBI 2017)*, Melbourne, Australia, April 2017.

[14] S. Liu, S. Liu, W. Cai et al., "Multimodal neuroimaging feature learning for multiclass diagnosis of Alzheimer's disease," *IEEE Transactions on Biomedical Engineering*, vol. 62, no. 4, pp. 1132–1140, 2015.

[15] S. H. Nozadi and S. Kadoury, "Classification of Alzheimer's and MCI patients from semantically parcelled PET images: a comparison between AV45 and FDG-PET," *International Journal of Biomedical Imaging*, vol. 2018, Article ID 1247430, 13 pages, 2018.

[16] Y. Gupta, R. K. Lama, and G.-R. Kwon, "Prediction and classification of Alzheimer's disease based on combined features from apolipoprotein-E genotype, cerebrospinal fluid, MR, and FDG-PET imaging biomarkers," *Frontiers in Computational Neuroscience*, vol. 13, p. 72, 2019.

[17] T. H. Gorji and K. Naima, "A deep learning approach for diagnosis of mild cognitive impairment based on MRI images," *Brain Sciences*, vol. 9, no. 9, p. 217, 2019.

[18] D. Chyzhyk, M. Graña, A. Savio, and J. Maiora, "Hybrid dendritic computing with kernel-LICA applied to Alzheimer's disease detection in MRI," *Neurocomputing*, vol. 75, no. 1, pp. 72–77, 2012.

[19] T. Zhang, Z. Zhao, C. Zhang, J. Zhang, Z. Jin, and L. Li, "Classification of early and late mild cognitive impairment using functional brain network of resting-state fMRI," *Frontiers in Psychiatry*, vol. 10, p. 572, 2019.

[20] R. Cuingnet, E. Gerardin, J. Tessieras et al., "Automatic classification of patients with Alzheimer's disease from structural MRI: a comparison of ten methods using the ADNI database," *NeuroImage*, vol. 56, no. 2, pp. 766–781, 2011.

[21] S. Farhan, M. A. Fahiem, and H. Tauseef, "An ensemble-of-classifiers based approach for early diagnosis of Alzheimer's disease: classification using structural features of brain images," *Computational and Mathematical Methods in Medicine*, vol. 2014, Article ID 862307, 11 pages, 2014.

[22] Y. Cho, J.-K. Seong, Y. Jeong, and S. Y. Shin, "Individual subject classification for Alzheimer's disease based on incremental learning using a spatial frequency representation of cortical thickness data," *NeuroImage*, vol. 59, no. 3, pp. 2217–2230, 2012.

[23] R. Wolz, V. Julkunen, J. Koikkalainen et al., "Multi-method analysis of MRI images in early diagnostics of Alzheimer's disease," *PLoS One*, vol. 6, no. 10, Article ID e25446, 2011.

[24] C. Ledig, R. A. Heckemann, A. Hammers et al., "Robust whole-brain segmentation: application to traumatic brain injury," *Medical Image Analysis*, vol. 21, no. 1, pp. 40–58, 2015.

[25] K. Van Leemput, F. Maes, D. Vandermeulen, and P. Suetens, "Automated model-based tissue classification of MR images of the brain," *IEEE Transactions on Medical Imaging*, vol. 18, no. 10, pp. 897–908, 1999.

[26] C. Ledig, "Segmentation of MRI brain scans using," in *Proceedings of the MICCAI 2012 Grand Challenge and Workshop on Multi-Atlas Labeling*, Nice, France, September 2012.

[27] A. H. Andersen, D. M. Gash, and M. J. Avison, "Principal component analysis of the dynamic response measured by fMRI: a generalized linear systems framework," *Magnetic Resonance Imaging*, vol. 17, no. 6, pp. 795–815, 1999.

[28] J. Cohen, "A coefficient of agreement for nominal scales," *Educational and Psychological Measurement*, vol. 20, no. 1, pp. 37–46, 1960.

[29] M. L. McHugh, "Interrater reliability: the kappa statistic," *Biochemia Medica*, vol. 22, pp. 276–282, 2012.

[30] F. Deng, S. Siersdorfer, and S. Zerr, "Efficient jaccard-based diversity analysis of large document collections," in *Proceedings of the 21st ACM International Conference on*

Information And Knowledge Management-CIKM '12, p. 1402, Maui, HI, USA, 2012.

[31] A. Patil and N. S. Upadhyay, "Restaurant's feedback analysis system using sentimental analysis and data mining techniques," in *Proceedings of the 2018 International Conference on Current Trends Towards Converging Technologies (ICCTCT)*, IEEE, Coimbatore, Tamilnadu, India, pp. 1–4, March 2018.

Hindawi
Journal of Healthcare Engineering
Volume 2020, Article ID 7914649, 14 pages
https://doi.org/10.1155/2020/7914649

Research Article

Sensor Type, Axis, and Position-Based Fusion and Feature Selection for Multimodal Human Daily Activity Recognition in Wearable Body Sensor Networks

Abeer A. Badawi,[1] Ahmad Al-Kabbany,[1,2,3] and Heba A. Shaban[1]

[1]*Electronics and Communications Engineering Department, Arab Academy for Science, Technology & Maritime Transport (AASTMT), Alexandria, Egypt*
[2]*Intelligent Systems Lab, Arab Academy for Science, Technology & Maritime Transport, Abu Kir Campus, Alexandria, Egypt*
[3]*Department of Research and Development, VRapeutic, Cairo, Egypt*

Correspondence should be addressed to Ahmad Al-Kabbany; alkabbany@ieee.org

Received 2 August 2019; Revised 15 April 2020; Accepted 9 May 2020; Published 8 June 2020

Academic Editor: Belayat Hossain

This research addresses the challenge of recognizing human daily activities using surface electromyography (sEMG) and wearable inertial sensors. Effective and efficient recognition in this context has emerged as a cornerstone in robust remote health monitoring systems, among other applications. We propose a novel pipeline that can attain state-of-the-art recognition accuracies on a recent-and-standard dataset—the Human Gait Database (HuGaDB). Using wearable gyroscopes, accelerometers, and electromyography sensors placed on the thigh, shin, and foot, we developed an approach that jointly performs sensor fusion and feature selection. Being done jointly, the proposed pipeline empowers the learned model to benefit from the interaction of features that might have been dropped otherwise. Using statistical and time-based features from heterogeneous signals of the aforementioned sensor types, our approach attains a mean accuracy of 99.8%, which is the highest accuracy on HuGaDB in the literature. This research underlines the potential of incorporating EMG signals especially when fusion and selection are done simultaneously. Meanwhile, it is valid even with simple off-the-shelf feature selection methods such the Sequential Feature Selection family of algorithms. Moreover, through extensive simulations, we show that the left thigh is a key placement for attaining high accuracies. With one inertial sensor on that single placement alone, we were able to achieve a mean accuracy of 98.4%. The presented in-depth comparative analysis shows the influence that every sensor type, position, and placement can have on the attained recognition accuracies—a tool that can facilitate the development of robust systems, customized to specific scenarios and real-life applications.

1. Introduction

Accurate and timely recognition of human daily activities, throughout the day, is required in remote health-monitoring and care-giving systems [1]. One approach for recognizing human activities is to analyze the biosignals acquired using on-body sensors, which has been addressed by a significant body of research to date [2]. This attention has been stimulated by several factors, including the advances in machine learning techniques. These techniques represent a powerful tool for figuring out patterns in the biosignals, with which they can be differentiated and thus recognized. The literature has witnessed several datasets which are constructed to facilitate effective and efficient model learning, with interdataset variations that include the number of subjects, the types of sensors, and the positions of sensors, in addition to others [3]. Efficient inference using the learned models has necessitated the identification of the most indicative features in the dataset. This can be done using feature selection techniques which have been used often to simplify the learned models, reduce the computational complexity in real-life applications, and enhance the recognition accuracies as well.

In this work, we employ the Human Gait Database (HuGaDB) [4]. This is a recently constructed dataset which has several unique characteristics for studying human activity recognition. It provides biosignals acquired using three of the most widely used types of sensors in the field, namely, gyroscopes, accelerometers, and electromyography (EMG) sensors, placed on the left and right feet, shins, and thighs. Another reason for choosing such a dataset is that it considers the most comprehensive set of activities in the literature (twelve activities). It covers daily static and dynamic activities which represent a rich source of information that empowers effective model learning and thus accurate recognition.

Our own previous research [5] investigates the relation between the recognition accuracy and the IMU's placements-and-orientations [5]. We also highlight the impact (in terms of accuracy) of applying feature selection techniques on the IMU's data [6]. This research, however, studies the fusion of EMG sensor data with the IMU's data. Particularly, we incorporate our knowledge on the best sensor placements-and-orientations, in addition to our findings on the impact of feature selection, and we show that EMG data can influence the system's recognition capacity positively. In this work, we have considered widely used classifiers, namely, support vector machine (SVM), naive Bayes (NB), neural networks as multilayer perceptron (MLP), decision tree (DT), *k*-nearest neighbor (*k*-NN), and random forest (RF) [5]. We have also followed the study in [6] while applying feature selection. Hence, we used the different approaches for sequential feature selection including sequential forward feature selection (SFS), sequential backward feature selection (SBS), and sequential forward floating feature selection (SFFS) [6].

The contributions of this research can be summarized as follows:

(1) Identifying, for each sensor (accelerometer, gyroscope, and EMG), the direction and the sensor position that achieved the highest accuracies for human activity recognition, in addition to the best classifier from the six different algorithms applied

(2) Demonstrating that using the best axis for a sensor, together with the best classifier and selected features, can lead to a competitive performance that is close to the performance achieved considering the whole three axes of that sensor

(3) Showing that feature selection methods yield a significant improvement in the recognition accuracies, with an approximate of half the number of the original features retained

(4) Attaining the highest recognition accuracy on HuGaDB using sensor fusion (of accelerometers, gyroscope, and EMG) and off-the-shelf feature selection technique

The rest of this article is structured as follows. Section 2 highlights the literature review. A discussion on the used dataset and the methods used for data processing is provided in Section 3. Section 4 gives numerical results. Finally, the conclusion is provided in Section 5.

2. Related Work

Wearable sensors, such as accelerometers and gyroscopes, are widely used for human activity recognition. Because accelerometers measure linear acceleration, they fail to identify actions that are characterized by (or involve) joint rotation. Hence, combining gyroscopes, which measure rotational motion, with accelerometers can overcome such a problem. These two sensors are normally integrated in one wearable inertial mobile unit (IMU).

Another type of wearable sensors is the surface electromyography (sEMG). The myoelectric signal measured by the sEMG represents the electrical current associated with muscular action; hence, it can play an important role in activity recognition. In this study, we consider wearable inertial sensors and sEMG sensors placed on different positions of the body. In addition, we consider other major aspects of comparison including the number of subjects, features, activities, sensor placements, and types, and finally the various types of classifiers (the machine learning algorithms) used.

Among the previous work on human activity recognition is the scheme presented in [7]. The study involved 10 participants, each performed 7 activities, and the signals were collected from accelerometers on the ankle and the wrist. Eleven features were extracted from the signals corresponding to each activity, and finally, *k*-NN and artificial neural networks were used as classifiers, which achieved an accuracy of 97%. In pursuit of the highest recognition accuracies, the authors of [8] investigated different classification techniques, such as SVM, regularized linear regression, and Adaboost. These methods were used to classify 7 different activities from 10 subjects, and 5 features were extracted from accelerometers placed on 3 different places on the body. Finally, the average accuracy for subject-independent, subject-adaptive, and subject-dependent accuracies was 78.2% from Adaboost.

A novel method was proposed for activity identification in [9], with 15 subjects and 3 sensors; 18 actions were performed, and accelerometers were used with 4 features extracted from the signal. Finally, a decision tree algorithm is used to classify the activities, and it attained a 93.8% accuracy.

In [10], the adopted setup involved accelerometers on 4 different body positions to recognize 5 activities, and 4 subjects participated in the study. The authors extracted 12 features, and 3 machine learning algorithms were used for classification. The accuracy was calculated per subject, and the average accuracy for the three subjects and one subject vs all is 81% using the HMM classifier.

In the context of activity classification, the performance on two datasets was compared in [11]. The first dataset used accelerometer readings from the chest during a walking activity from 18 subjects, with 9 features extracted. The reported average accuracy was 99.8% using random forest, just for the walking activity. The second dataset consisted of six activities from 30 subjects, collected using accelerometers and gyroscopes, where the signals were collected from the waist. The study included 10 classification algorithms that

were applied on 24 features and attained an average accuracy per activity that equals to 99.9%.

Surface electromyography (sEMG) and accelerometer sensors were used for monitoring daily activities of stroke patients in [12]. The sEMG and accelerometer data were recorded from 10 patients while doing 11 activities. The data prediction stage of the proposed pipeline was done using a multilayered neural network. The author calculated the sensitivity and specificity. Hence, we used both of these figures to compute the accuracy, which reached 97.4%, in order to be able to compare it with the literature.

The research in [13] introduced MyoGym which included 8 electromyogram sensors and a 9-axis unit containing 3-axis gyroscope, 3-axis accelerometer, and 3-axis magnetometer. The data were collected from 10 subjects, performing 30 different gym activities. Linear discriminant analysis (LDA) and quadratic discriminant analysis (QDA) were used to classify the different activities. The accuracy for all sensors combined together was 71.6% using LDA.

Recently, a new method was proposed in [14] to recognize human activities based on a feature selection approach. The signals corresponding to 13 different activities were collected using accelerometers and gyroscopes from the ankle, wrist, hip, and chest. Nineteen different features were extracted and only k-NN was used for classification, and it attained 99.13% accuracy. Another method for dynamic segmentation of features was proposed in [15]. An accelerometer sensor placed on the wrist was used to predict 12 different activities from 10 subjects, and finally, 14 features were extracted for classification using the following methods: DT, SVM, *k*-NN, MLP, and NB, with 94.21% accuracy attained using SVM.

In [16], two datasets were used for activity recognition. The first dataset involved 31 subjects, and the second dataset involved 30 subjects. In both datasets, accelerometers and gyroscopes were located on the waist. Also, the participants performed 6 different activities, and 17 features were adopted. This research involved two classifiers, namely, SVM and RF, with 5 types of ensemble classifiers—Bagging, Rotation Forest, Adaboost, Random Subspace, and Ensembles of Nested Dichotomies. The highest accuracies attained were 95.33% using the SVM classifier for the first dataset and 99.22% for the second dataset. Finally, a literature review was released in 2018 for sensor-based datasets that were constructed for human activity recognition [3]. It reviews the various types of sensors and devices used in the literature. There are three datasets that are related to our research, namely, UCI-HAR dataset [17], Opportunity AR dataset [18], and mHEALTH [19].

In this research, we use 3 types of sensor data (accelerometer, gyroscope, and electromyography) and six classification techniques to classify the activities, in addition to four feature selection algorithms. Also, 12 activities and 7 different sensor placements, with 18 subjects, are considered. According to the literature survey presented earlier, and the summary in Table 1, this study has three merits:

(1) It investigates the effectiveness of the electromyography sensor when it is combined with accelerometer and gyroscope sensors to recognize human activities

(2) It presents a thorough comparison between the different types of commonly used machine learning techniques and feature selection methods, while at the same time, taking into consideration other aspects of comparison, such as the number of subjects and activities

(3) It achieves a significantly high accuracy (99.8%) on a recent-and-comprehensive dataset

In Table 1, we summarize the most recent and pertinent work in the literature. The comparison includes studies that adopted accelerometers alone, or accelerometers with gyroscopes and electromyography. In our comparison, we also included the number of subjects, activities, features, sensor position, classification methods, and the average accuracy. We also show different performance metrics that were used by the pertinent literature in Table 2. It can also be seen from this table that accuracy is the most widely used metric in the literature.

3. Methodology

3.1. Dataset Description. The Human Gait Database (HuGaDB) by Roman Chereshnev is used in this work [4]. This dataset contains twelve activities, with the following ID numbers: walking with ID number [0], running with ID number [1], going down with ID number [2], going up with ID number [3], sitting with ID number [4], sitting down with ID number [5], standing up with ID number [6], standing with ID number [7], bicycling with ID number [8], down by elevator with ID number [9], up by elevator with ID number [10], and sitting in the car with ID number [11]. The data was collected from 18 adults (14 males and 4 females).

Six body inertial wearable sensors were located in the left and right shin, thigh, and foot with a total of six placements, for accelerometers and gyroscopes. Electromyography sensors were placed on vastus lateralis. The samples were collected from 3-axis accelerometer, 3-axis gyroscope, and surface electromyography (sEMG) sensors, which yield a total number of 38 signals, 36 signals from the inertial sensors and 2 signals from the sEMG sensor. In addition to being recent and well-documented, the choice to work on the HuGaDB dataset is inspired by the inertial nature of the sensors used to collect the signals. This enables us to study how the individual movements of the different parts of the two legs can help in predicting the human activity.

3.2. Data Preprocessing. Our proposed pipeline starts with a preprocessing stage which involves signal normalization and segmentation. Due to the difference in units and ranges of the collected data (from the 3 types of sensors), it was required to normalize it using zero-mean and unit variance as shown in the following equation:

Table 1: Review of the different techniques from the literature that are most-related to the proposed research.

Study	No. of subjects	No. of activities	No. of features	No. of positions	Sensor position	Sensor type	Classifiers	Average of classification accuracy
[7]	10	7	11	2	Wrist and ankle	Accelerometer	PNN and K-PNN	96%
[8]	10	7	5	3	Hip, thigh, and ankle	Accelerometer	SVM, regularized LR, and Adaboost	78.2%
[9]	15	18	4	3	Wrist, waist, and thigh	Accelerometer	Decision tree	93.8%
[10]	4	5	12	4	Left thigh, right arm, ankle, and abdomen	Accelerometer	SVM, AMM, HNN	81% avg. per subject
[11]	30	6	24	1	Waist	Accelerometer and gyroscope	RF, SVM, NB, J48, NN, K-NN, Rpart, JRip, Bagging, and Adaboost	99.8% avg. per activity
[11]	18	1	9	1	Chest	Accelerometer	NB, SVM, RF, J48, NN, K-NN, Rpart, JRip, Bagging, and Adaboost	99.9% avg. per activity
[12]	10	11	8	8	Arms, thigh, waist, and chest	Accelerometer and electromyography	ANN	97.4%
[13]	10	30	12	1	Arm	Accelerometer, gyroscope, magnetometer, and electromyography	LDA and QDA	71.6%
[14]	19	13	19	4	Chest, ankle, hip, and wrist	Accelerometer and gyroscope	k-NN	99.13%
[15]	10	12	14	1	Wrist	Accelerometer	DT, SVM, k-NN, MLP, and NB	96.87%
[16]	30	6	17	1	Waist	Accelerometer and gyroscope	SVM and RF	99.22%
[16]	31	6	17	1	Waist	Accelerometer and gyroscope	SVM and RF	95.33%
[17]	30	6	5	1	Waist	Accelerometer and gyroscope	Multiple HMMs, MOT, and k-NN	92.6%
[18]	4	4	—	14	Upper body, leg, and hip	Inertial sensors and accelerometers	DL (NMF + SAE)	99.9%
[19]	10	12	—	3	Chest, right wrist, and left ankle	Accelerometer, ECG, gyroscope and magnetometer	Hierarchical classification method HCM	97.2%
Ours	18	12	14	7	Right and left thighs, right and left shins, and right and left feet and an EMG on the thigh	Accelerometer, gyroscope and EMG	Neural networks, naive Bayes, random forest, (k-NN), SVM, and decision trees	99.8%

$$f_{\text{norm}} = \frac{f_{\text{raw}} - \mu}{\sigma}, \quad (1)$$

where μ and σ are the mean and standard deviation, respectively.

Following the literature, most of the activity classification methods use windowing techniques for dividing a time-series signal into smaller segments. In this work, we use time-based sliding windows with 50% data overlap [20]. This overlap percentage is commonly used for activity recognition and was shown to yield the highest recognition accuracies [21].

3.3. Feature Extraction and Selection. Accurate and efficient activity recognition requires the selection of the most relevant features and/or the removal of redundant information. The two steps of feature extraction and selection are meant to serve this purpose. In this research, we adopt the commonly used statistical and time domain-based features proposed in the literature for accurate human activity recognition (HAR) [22, 23]. Table 3 shows the features used, their definitions, and the signals from which we extracted those features [24–26].

Table 2: Review of the different performance metrics that were used with pertinent techniques in the literature.

Study	Accuracy (%)	$F1$-score	Precision	Recall	CV method	Sensitivity (%)	Specificity (%)
[7]	96	—	—	—	Leave-one-out (LOOCV)	—	—
[8]	78.2	—	—	—	10-fold CV	—	—
[9]	93.8	—	—	—	Leave-one-out (LOOCV)	—	—
[10]	81	—	—	—	Leave-one-out (LOOCV)	—	—
[11]	99.8	—	—	—	5-fold CV	100	100
[12]	97.4	—	—	—	—	95	99.7
[13]	71.6	—	—	—	—	—	—
[14]	99.13	Avg. of all activities 98.86%	Avg. of all activities 98.77%	Avg. of all activities 98.95%	Leave-one-out (LOOCV)	—	—
[15]	96.87	85.84%	—	—	10-fold CV	84.7	85.3
[16]	99.22	Avg. of all activities 99.23%	Avg. of all activities 99.23%	Avg. of all activities 99.23%	10-fold CV	—	—
[16]	95.33	Avg. of all activities 95.52%	Avg. of all activities 95.52%	Avg. of all activities 95.50%	10-fold CV	—	—
[17]	92.6	—	—	—	—	—	—
[18]	99.9	99.4%	99.4%	99.4%	Leave-one-out (LOOCV)	—	—
[19]	97.2	97.2%	97.2%	97.2%	—	—	—
Ours	99.8	99.3%	99.1%	99.4%	10-fold CV	99.4	99.1

Table 3: Definition of the features extracted in the proposed research.

Feature	Description
Standard deviation	Standard deviations of (x, y, z, magnitude) from accelerometer, gyroscope signals, and EMG signal
Standard deviation Auto-correlation	Auto-correlation of the standard deviations of (x, y, z, magnitude) from accelerometer, gyroscope signals, and EMG signal *Adopted function*: statsmodels.tsa.stattools.acf (x, unbiased = false, nlags = 40, qstat = false, fft = none, alpha = none, missing = "none")
Standard deviation Auto-covariance	Auto-covariance of the standard deviations of (x, y, z, magnitude) from accelerometer, gyroscope signals and EMG signal *Adopted function*: statsmodels.tsa.stattools.acv (x, unbiased = false, nlags = 40, qstat = false, fft = none, alpha = none, missing = "none")
Variance	Variance of (x, y, z, magnitude) from accelerometer, gyroscope signals, and EMG signal
Mean	Mean of (x, y, z, magnitude) from accelerometer, gyroscope signals, and EMG signal
Mean Auto-covariance	Auto-covariance of the mean values of (x, y, z, magnitude) from accelerometer, gyroscope signals, and EMG signal
Mean Auto-correlation	Auto-correlation of the mean values of (x, y, z, magnitude) from accelerometer, gyroscope signals, and EMG signal
Minimum	Minimum value of (x, y, z, magnitude) from accelerometer, gyroscope signals, and EMG signal
Maximum	Maximum value of (x, y, z, magnitude) from accelerometer, gyroscope signals, and EMG signal
Skewness	Asymmetry of (x, y, z, magnitude) from accelerometer, gyroscope signals, and EMG signal *Adopted function*: scipy.stats.skew (a, axis = 0, bias = true)
Kurtosis	Fourth central moment value divided by the variance square value of (x, y, z, magnitude) from accelerometer, gyroscope signals, and EMG signal *Adopted function*: scipy.stats.skew (a, axis = 0, bias = true)
Root-mean squared	Square root of the mean square (x, y, z, magnitude) from accelerometer, gyroscope signals, and EMG signal
Mean crossing rate	Mean crossing rate of (x, y, z, magnitude) from accelerometer, gyroscope signals, and EMG signal
Jitter	Jitter of (x, y, z, magnitude) from accelerometer, gyroscope signals, and EMG signal, where the jitter is defined as the deviation of a signal's significant instants from their ideal positions in time

Feature selection is commonly used for dimensionality reduction. In this research, we aim to investigate the impact of sequential feature selection (SFS) algorithms on the recognition accuracy. Particularly, we adopt the following feature selection methods: (1) sequential backward selection, (2) sequential forward selection, (3) sequential backward floating selection (SBFS), and (4) sequential forward floating selection (SFFS). The notable merit of the SFS family of algorithms is their simple implementation. Basically, this group of greedy algorithms sequentially adds one feature at a time and retains that feature if it yields a better classification accuracy [27]. SFFS and SBFS implement the forward and backward step at every iteration to ensure that the feature selected is the best with the previous and the next subset of features.

3.4. Classification Techniques. In this work, we recognize activities in the HuGaDB dataset using a set of well-studied machine learning techniques, namely, multilayer perceptron (MLP), naive Bayes (NB), random forest (RF), k-nearest neighbor (k-NN), support vector machine (SVM), and decision tree (DT). As was mentioned in Section 2, these techniques are widely used in the field of activity recognition from wearable sensors. The reported performance in this study is based on the accuracy and a 10-fold cross validation.

3.5. Signal-Processing Method. We elaborate below on the pipeline of the proposed system, which is composed of three stages. To justify each step, we show the impact it has on the ultimate recognition accuracies. Stage one aims to classify the activities from accelerometer and gyroscope sensors to find the best classifier and the most revealing sensor placement. Stage two is meant to highlight the effect of using feature selection. Finally, the last stage aims to investigate the fusion of the outputs of the three sensors, namely, accelerometer, gyroscope, and electromyography sensor. Figure 1 shows the pipeline of the proposed method. We elaborate on it in the following points:

(1) The dataset used in our research is collected from the thigh, foot, and shin for both left and right legs. Accelerometer and gyroscope signals contain (x, y, z) components. Their magnitude is also added as a feature.

(2) Each sensor detects twelve different signals that correspond to the different activities from eighteen subjects.

(3) Each signal is then normalized to have the same range for all sensors, and then a fixed-length window is applied to each signal with 100 samples and a 50% overlap.

(4) Next, we extract 14 features from each window.

(5) The optimal number of features is computed from the signals by applying the four different types of sequential feature selection to select the most important information. Each signal obtained different number of features to achieve the highest accuracy.

(6) We divide the dataset to a 70–30 ratio for training and testing to apply the aforementioned six machine learning algorithms.

(7) Fusion of sensors is then implemented between the accelerometer-and-gyroscope signals and the electromyography signal. Electromyography signal goes throw the same aforementioned steps before getting fused with other sensors.

(8) Investigating the fusion between sensors is done according the three following approaches: (1) accelerometer and electromyography signals, (2) gyroscope and electromyography signals, and (3) accelerometer, gyroscope, and electromyography signals.

4. Results and Discussion

We dedicate this section to highlight the results attained by applying the machine learning classifiers that were discussed in Section 3, on the HuGaDB dataset. For simulations, the code was written in Python, and we used the Scikit-learn library for applying the different machine learning techniques. The 6 classification methods mentioned in Section 3 are applied on each axis and magnitude, position on the right and left legs, and the combination of the sensor parameters. Table 4 indicates the parameters we used for each of the adopted classifiers. We also compare the performance achieved using three aforementioned sensors accelerometer, gyroscope, and electromyography sensor, and the accuracies obtained from the optimal system. The discussion of the results starts by focusing on accelerometers and gyroscopes, and later in this section, we expand the presentation to involve the sEMG sensor. Furthermore, we discuss the impact of applying the SFS family of feature selection techniques on the recognition accuracy of the proposed system.

4.1. Performance Evaluation for Optimal Sensor Placement. To evaluate the best sensor placement, we considered the accelerometer and gyroscope sensors only, because of their ability to recognize the activities accurately as mentioned in our previous work [5]. The classification techniques were applied on the dataset of the inertial sensor placements, axes, and magnitude, in addition to the EMG sensor. As the inertial sensors are placed in three different placements on both legs, the total number attributes is 24 per leg, i.e., a total of 48 attributes for the left and right legs. Figure 2 depicts a boxplot for the accuracies of the left leg accelerometer (total of 24 attributes). The figure demonstrates that the highest accuracy attained from the different placements and orientations of left leg accelerometer is 90.7% using the random forest algorithm. This accuracy is obtained from the x-axis component of the accelerometer on the thigh. DT and SVM achieved 89.4% and 88.1%, respectively, on the accelerometer's data. The right leg showed almost similar accuracies. The results obtained in this section, with regards to the best sensor placement, will affect the rest of the pipeline as will be

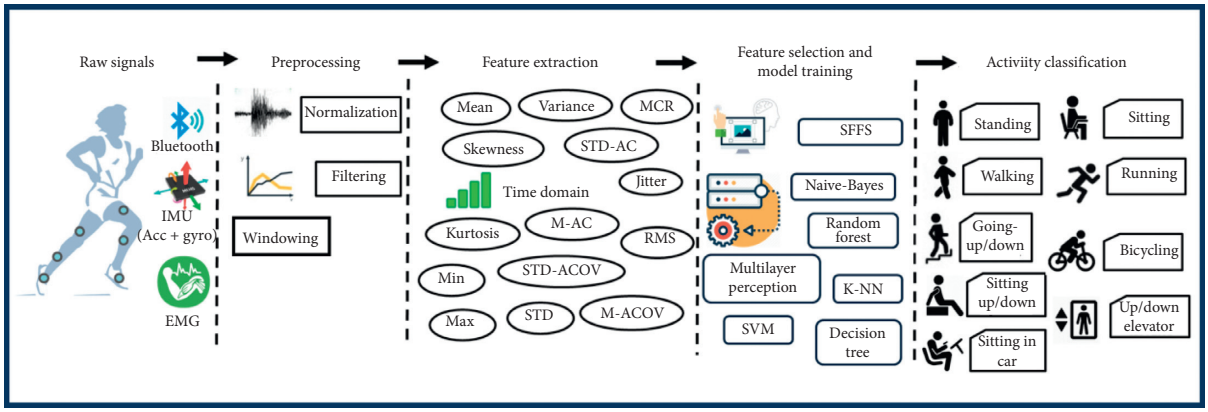

Figure 1: Scheme of the proposed system adopted in this research.

Table 4: Parameters of each of the adopted classifiers.

Classifiers	Parameters
Multilayer Perceptrom	sklearn.neural_network.MLPClassifier(hidden_layer_sizes = (100,), activation = "relu", solver = "adam", alpha = 0.0001, batch_size = "auto," learning_ate = "constant," learning_rate_init = 0.001, power_t = 0.5, max_iter = 200, shuffle = True, random_state = None, tol = 0.001, verbose = False, warm_start = False, momentum = 0.9, nesterovs_momentum = True, early_stopping = False, validation_fraction = 0.1, beta_1 = 0.9, beta_2 = 0.999, epsilon = $1e-08$, n_iter_no_change = 10, max_fun = 15000) We tested hidden_layer_sizes = (10, 20, 50, 75, 100) and hidden_layer_sizes = 100 gave best results
Decision tree (DT)	sklearn.tree.DecisionTreeClassifier(criterion = "gini," spliter = "best," max_depth = None, min_samples_split = 2, min_samples_leaf = 1, min_weight_fraction_leaf = 0.0, max_features = None, random_state = None, max_leaf_nodes = None, Min_impurity_decrease = 0.0, min_impurity_spilt = None, class_weight = None, presort = "deprecated." ccp_alpha = 0.0)
Random forest (RF)	sklearn.ensemble.RandomForestClassifier(n_estimators = 128, criterion = "gini," max_depth = None, min_samples_spilt = 2, min_samples_leaf = 1, min_weight_fraction_leaf = 0.0, max_features = "auto," max_leaf_nodes = None, min_impurity_decrease = 0.0, min_impurity_split = None, bootstrap = True, oob_score = False, n_jobs = None, random_state = None, verbose = 0, warm_start = False, class_weight = None, ccp_alpha = 0.0, max_samples = None) We tested n_estimators = (10, 64, 12, 256), and n_estimators = 256 gave best results. Homwever, there was aslight difference compared to n_estimators = 128. So, we applied 128 to reduce the over all running time
k-Nearest neighbors (k-NN)	kNeighborsClassifier(n_neighbors = 5, weights = "uniform," algorithm = "auto," leaf_size = 30, p = 2, metric = "minkowski," metric_params = None, n_jobs = None, **kwargs) We tested n_neighbors = (1, 5, 10, 20), and n_neighbors = 5 gave best results
Support vector machine (SVM)	sklearn.svm.SVC(C = 10, kernel = "linear," degree = 3, gamma = "auto," coef0 = 0.0, shrinking = True, probability = False, tol = 0.001, cache_size = 200, class_weight = None, verbose = False, max_iter = −1, decision_function_shape = "ovr," break_ties = False, random_state = None We tested C = 1, 10, 20, 50, 100 and Kernel = "rbf" and "linear," and the best results was obtained with gamma = "auto," C = 10, and kernel = "linear"
Naive Bayes	sklearn.naive_bayes.GaussianNB (priors = None, var_smoothing = $1e-09$)

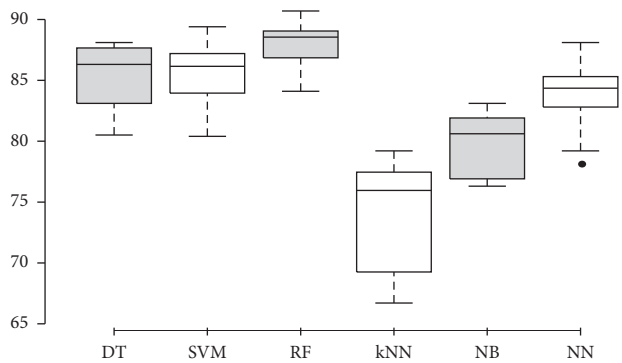

Figure 2: Boxplots of different classifiers' accuracies for data from accelerometer signals (please see text for more details).

shown in the following sections after adding the EMG sensor to these best positions and axes.

4.2. Optimal Classifier and Feature Selection Algorithm

4.2.1. Performance Evaluation for Optimal Classifier. First, we started by investigating the classification accuracies of the accelerometer and gyroscope sensors attained from the left leg. We compared between three different positions, namely, the foot (lf), the thigh (lt), and the shin (ls). The random forest (RF) has consistently outperformed the other classifiers, while the least effective classifiers are the *K*-NN and the naive Bayes. Although random forest, support vector machine, and decision tree classifiers have proven significant effectiveness, the RF classifier's interquartile range (IQR) shows superior consistency when varying the sensor positions compared to the other classifiers' IQR. Later in this discussion, we elaborate further on the superiority of the random forest classifier with regards to the consistency across varying sensor placements. It is worth mentioning that this aligns with other conclusions in the literature with regards to the superiority of the random forest classifier over other classifiers [5], followed by SVM and DT, and the same steps were repeated to observe the changes after the EMG sensor addition. Figure 3 shows the confusion matrix of the RF classifier. The predicted label activities versus the true label showed only three wrong detections:

(1) For ID 11 (sitting in the car), it was predicted as ID 6 (sitting) twice

(2) For ID 7 (standing), it was predicted as ID 8 (cycling)

(3) For ID 6 (sitting), it was predicted as ID 11 (sitting in the car)

The accuracy reached 98.6%, and this result was obtained from both types of sensors (accelerometers and gyroscopes) and by setting the random forest number of trees to 256 instead of 10 (10 is the default number of trees in Scikit-learn library).

4.2.2. Optimal Number of Features. This section presents a method for obtaining the optimal number of features. This is done by using cross-validation and the sequential feature selection family of algorithms, in order to score different feature subsets, and then choose the best number of features that attain the highest accuracy. The curve in Figure 4 shows a random example of our method. We chose the *y*-axis of the gyroscope sensor, and the figure shows that the curve reaches the maximum accuracy when $N = 8$, where N is the number of features. At that value of N, the variability in the performance is the least; also, it is followed by a gradual and almost-monotonic decline in the performance. The sky-blue shade above and below the blue curve shows the changing in the cross-validation, one standard deviation above and below the accuracy score shown in the curve. Our insight is that the decline following $N = 8$ is due to adding non-informative features to the model learning process. After investigating the performance of four sequential feature selection approaches, sequential forward floating feature selection attained the highest accuracy while retaining the minimum number of features compared to other methods. Those steps were repeated for the EMG signal on both legs to obtain the optimal number of features.

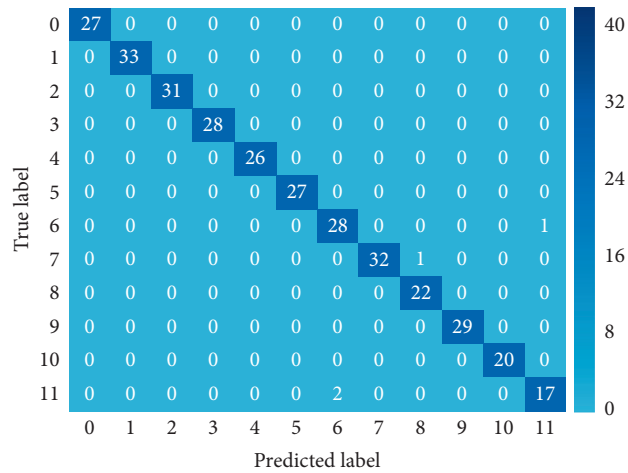

Figure 3: Confusion matrix for the random forest classifier from the accelerometer and the gyroscope sensors placed on the left thigh [5].

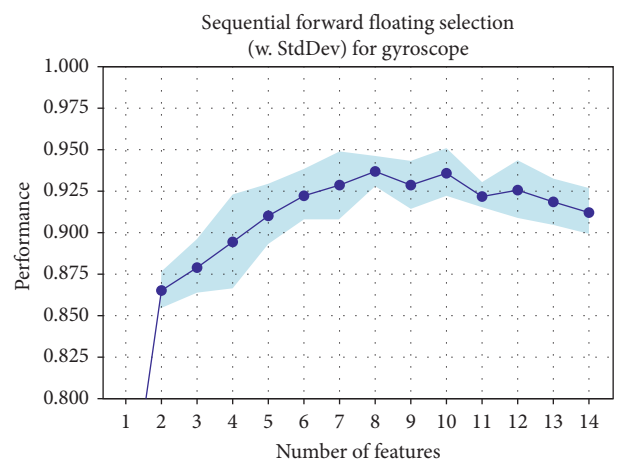

Figure 4: Gyroscope *y*-axis performance when the number of features is varied [6].

4.3. Comparison between Single Axis vs Triple Axes and All Features vs Selected Features.

After selecting the optimal number of features for the best position (thigh on the left leg), we compare the performance achieved using all proposed features and that obtained using the four types of sequential feature selection approaches (backward, forward, backward floating, and forward floating). In this experiment, we included the classifiers that achieved the highest recognition accuracies in the previous experiments, support vector machine, random forest, k-NN, and the one that attained the least accuracies (decision tree). The comparison highlights the best output we obtained in Sections 4.1 and 4.2:

(1) The best axis, namely, the x-axis for the accelerometer sensor and the y-axis for gyroscope sensor, both obtained from the left thigh

(2) The combination of the best axes (x, y, and z axes and their magnitude)

Table 5 shows the classification accuracies obtained by the classifiers, before using feature selection, on the following sensor placements: x-axis of accelerometer (A_lt_x), y-axis of gyroscope (G_lt_y), and their combination (A_lt_x and G_lt_y). It also shows the accuracies after combining all the axes and their magnitude (A, G_lt_x, y, z, and mag) of both sensors. Finally, the last column shows the total number of features used in each try.

As mentioned earlier [6] and boldfaced in Table 5, the best accuracy is achieved using the RF classifier. The best single axis achieved 94.7% with 28 features, and the combination of all parameters achieved 96.8% with 112 features. Table 6 shows the same comparison with feature selection taken into consideration. Our experiments showed that sequential forward floating feature (SFFS) selection outperforms other feature selection techniques. Table 6 shows that using feature selection leads to higher classification accuracy than that with all features obtaining 96.9% with 15 features selected from the single axis and 98.4% with 37 features selected from all parameters.

To conclude this part of the results, we showed that using feature selection, higher recognition accuracies can be attained with an average 50% reduction in the total number of features as mentioned in [6]. We adopted the four types of the sequential feature selection family of techniques, which outperformed all other approaches. The comparison between the performance achieved using sensor data from the single axis and triple axes demonstrated that the single axis can be used and still achieve high accuracies to detect the activities, even though there is an information gain from using the data of the three axes. Furthermore, a comparison between accuracies before and after using feature selection showed a significant performance enhancement after eliminating redundant or noninformative features. We build up on the previous conclusion by determining the most informative features and then applying the different classifiers on the data of the best sensor position and direction.

4.4. Investigating the Impact of Fusing the EMG Data with Accelerometers and Gyroscopes. Comparison between accelerometers, gyroscopes, and electromyography sensor data for activity recognition have not received significant research attention in the literature. Specifically, the use of EMG sensors for daily activity recognition placed at different positions of the body has not received much attention. Figure 5 shows a comparison between the classification accuracies of the six investigated classifiers and three types of sensor data without sensor data-fusion. As can be seen, EMG signal's classification accuracies are too low when used alone. This justifies the reason for not being widely used for activity recognition. However, EMG signals are important for applications that require muscle activity monitoring such as tele-rehabilitation. Accordingly, we investigate the impact of fusing the data from these three sensors on the accuracy of activity recognition. This section will be divided as follows: First, we compare the output of using jointly the data from accelerometers and electromyography sensor data to that of using the gyroscopes and electromyography sensor data. Finally, we discuss the fusion of these three sensor data with regards to accuracy, single axis versus triple axes, and the number of features after sensor fusion.

Table 5: Comparison between accuracies attained using single axis and triple axes before using feature selection.

Sensor type and position	DT	SVM	RF	k-NN	Number of features
A_lt_x	88.10	89.40	90.70	79.10	14
G_lt_y	85.80	83.90	86.80	66.90	14
A_lt_x and G_lt_y	90.00	89.40	**94.70**	71.50	28
A, G_lt_x, y, z and mag	95.10	95.40	**96.80**	84.80	112

Table 6: Comparison between accuracies attained using single axis and triple axes after using feature selection.

Sensor type and position	DT	SVM	RF	k-NN	Number of features
A_lt_x	89.80	91.50	91.67	82.00	7
G_lt_y	88.10	85.20	88.70	87.80	8
A_lt_x and G_lt_y	91.60	91.20	**96.90**	75.00	15
A, G_lt_x, y, z, and mag	96.40	97.00	**98.40**	86.30	37

4.4.1. Accelerometer and Electromyography Sensor Data. Accelerometers measure the linear acceleration that is applied to a device on all three axes (x, y, and z), including the force of gravity. However, electromyography is the collective electric signal from the muscles, which is managed by the nervous system and is produced while muscles contract. For the joint consideration of accelerometers and EMG sensor data, we repeat the same steps followed to generate the results in Tables 5 and 6. We compare between the best single axis of the accelerometer (left thigh x-axis) with the electromyography signal on one side and all the parameters of the accelerometer (x, y, z, and magnitude (mag)) with the electromyography signal on the other side.

Based on the conclusion in the previous section, we add our feature selection technique to the pipeline, in order to observe the improvement of the accuracies when the number of redundant or the noninformative features get eliminated. In Tables 7 and 8, it is shown that the x-axis component of the accelerometer and electromyography (A_lt_x + EMG) achieve a 92.31% accuracy using 28 features. On the other hand, using sequential forward floating selection obtains a 94.52% accuracy with only 16 features. Adding all accelerometer parameters to the electromyography signal (A_lt_all and EMG), the accuracy reaches 97.31% versus 98.22% after using feature selection; the

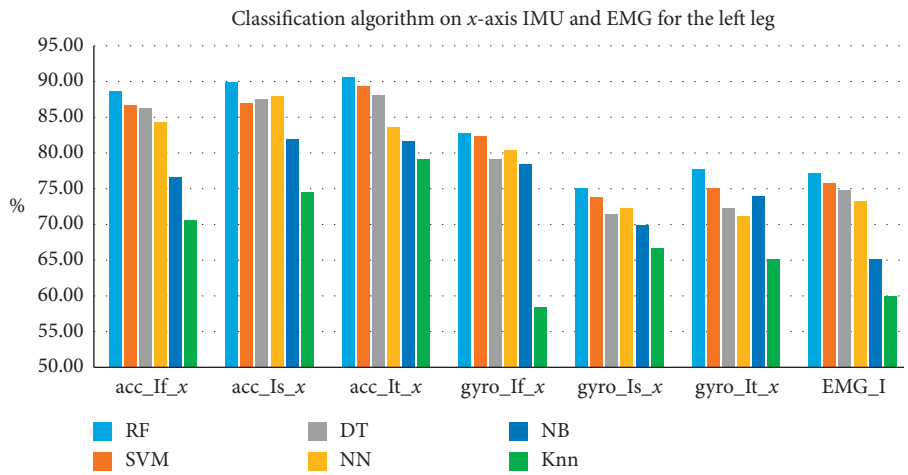

Figure 5: Six classification algorithm accuracies when applied on the x-axis signal from the foot, thigh, and shin of the left leg accelerometer, gyroscope, and EMG.

Table 7: Comparison between accuracies attained using single axis and triple axes for accelerometer and electromyography signals without using feature selection.

Sensor type and position	DT	SVM	RF	k-NN	Number of features
A_lt_x	88.10	89.40	90.70	79.10	14
EMG	76.90	78.90	79.20	66.20	14
A_lt_x + EMG	87.45	85.19	**92.31**	67.17	28
A_lt_all	92.03	93.60	95.00	83.90	56
A_lt_all + EMG	93.65	92.87	**97.13**	84	70

Table 8: Comparison between accuracies attained using single axis and triple axes for accelerometer and electromyography signals with sequential forward floating feature selection.

Sensor type and position	DT	SVM	RF	k-NN	Number of features
A_lt_x	89.80	91.50	91.67	82	7
EMG	78.00	80.30	84.30	70.10	11
A_lt_x + EMG	88.91	87.65	**94.52**	70.22	16
A_lt_all	94.20	95.10	96.20	85.10	23
A_lt_all + EMG	95.65	95.01	**98.22**	85.83	30

corresponding number of features were 70 and 30, respectively.

4.4.2. Gyroscope and Electromyography Sensor Data. Gyroscope measures the rate of a device rotation in rad/sec around each of the three axes (x, y, and z). With the results discussed below, we observe the relation between gyroscopes and electromyography sensors in the context of their ability to detect the muscle behaviour in addition to the muscle rotation and direction. We also observe the impact of the joint usage of these two sensors with and without feature selection. Although gyroscope and electromyography signals did not perform perfect separately, their combination leads to significant results. As shown in Table 9, random forest obtains the highest accuracy. The combination of data from the gyroscope's best single axis (y-axis) and the electromyography sensor (G_lt_y + EMG) achieves a 93.11% accuracy with 28 features. Considering all the gyroscope parameters jointly with EMG (G_lt_all + EMG), though, leads to a 95.41% accuracy with 70 features. On the other hand, our best feature selection algorithm (SFFS) decreases the number of features to 18 features for the best single axis for the gyroscope with the electromyography signals and still attains a 94.91% accuracy. Adopting feature selection with all the gyroscope parameters in addition to electromyography, the corresponding accuracy reaches 97.6% with 32 features only as shown in Table 10.

4.4.3. Accelerometer, Gyroscope, and Electromyography Sensor Data. Finally, we study the fusion of the data gathered from three types of sensor data, in order to investigate how the different features from these heterogeneous signals interact together. The major three comparisons highlighted in our discussion are the performance corresponding to data from single axis versus triple axes, the number of adopted features, and the optimal sensor fusion output. We present these comparisons in Tables 11 and 12. Table 11 demonstrates the results of combining the

Table 9: Comparison between accuracies attained using single axis and triple axes for gyroscope and electromyography signals without using feature selection.

Sensor type and position	DT	SVM	RF	k-NN	Number of features
G_lt_y	85.80	83.90	86.80	66.90	14
EMG	76.90	78.90	79.20	66.20	14
G_lt_y + EMG	88.60	90.41	**93.11**	72.96	28
G_lt_all	87.90	88.60	92.50	81.20	56
G_lt_all + EMG	90.27	90.83	**95.41**	73.10	70

Table 10: Comparison between accuracies attained using single axis and triple axes for gyroscope and electromyography signals with sequential forward floating feature selection.

Sensor type and position	DT	SVM	RF	k-NN	Number of features
G_lt_y	88.10	85.20	88.70	87.80	8
EMG	78.00	80.30	84.30	70.10	11
G_lt_y + EMG	90.11	91.78	**94.91**	75.23	18
G_lt_all	89%	90.10	94.40	82.90	26
G_lt_all + EMG	93.13	92.83	**97.60**	76.32	32

Table 11: Comparison between single axis vs triple axes for accelerometer, gyroscope, and electromyography signals before using feature selection.

Sensor type and position	DT	SVM	RF	k-NN	No. of features
A_lt_x	88.10	89.40	90.70	79.10	14
G_lt_y	85.80	83.90	86.80	66.90	14
EMG	76.90	78.90	79.20	66.20	14
A_lt_x + G_lt_y	90.00	89.40	94.70	71.50	28
A_lt_x + G_lt_y + EMG	91.40	90.70	**95.20**	72.80	42
A_lt_all	92.03	93.60	95.00	83.90	56
G_lt_all	87.90	88.60	92.50	81.20	56
A, G_lt_all	95.10	95.40	96.80	84.80	112
A, G_lt_all + EMG	96.80	96.70	**98.50**	87.30	126

Table 12: Comparison between accuracies attained using single axis and triple axes for accelermoeter, gyroscope, and electromyography signals with sequential forward floating feature selection.

Sensor type and position	DT	SVM	RF	k-NN	No. of features
A_lt_x	89.80	91.50	91.67	82	7
G_lt_y	88.10	85.20	88.70	87.80	8
EMG	78.00	80.30	84.30	70.10	11
A_lt_x + G_lt_y	91.60	91.20	96.90	75.00	15
A_lt_x + G_lt_y + EMG	93.10	92.40	**97.10**	78.40	24
A_lt_all	94.20	95.10	96.20	85.10	23
G_lt_all	89	90.10	94.40	82.90	26
A, G_lt_all	96.40	97	98.40	86.30	37
A, G_lt_all + EMG	97.30	98	**99.80**	88.10	45

data from the best single axis for accelerometer and gyroscope together with the electromyography signal (A_lt_x + G_lt_y + EMG). The joint usage of the previous features yields a recognition accuracy of 95.20% with 42 features. Furthermore, by considering all the accelerometer and the gyroscope parameters with the EMG (left thigh acc + gyro all + EMG), the accuracy reaches 98.50% with a total of 126 features. Table 12 features the same comparison

Table 13: Comparison between 10-fold CV and LOPO CV for accelerometer, gyroscope, and EMG sensors before applying feature selection.

Classifier/validation protocol	10-fold CV (%)	LOPO CV (%)
Random forest	98.5	98.9
SVM	96.7	96.5
Decision tree	96.8	96.3
KNN	87.3	86.8

in Table 9 while applying sequential forward floating feature selection. An accuracy of 97.1% is attained with 24 features only from the data of the single best axis, while 99.8% accuracy is attained with a total of 45 features from the data of all axes plus their magnitude in addition to the EMG signal. Table 13 and Table 14 highlight the influence of changing the adopted validation protocol on the attained accuracy before and after applying feature selection.

The results presented in this section are summarized in Figures 6 and 7, as they illustrate the relation between the accuracy and number of features. We highlight the most significant outputs in our work in these points:

(1) The best single axis and position that yield the highest accuracy, for the accelerometer and the gyroscope

(2) Fusion between electromyography, and accelerometer, and gyroscope best single axis

(3) Accelerometer and gyroscope fusion with all parameters (x, y, z, and magnitude)

(4) Fusion between electromyography with all accelerometer and gyroscope parameters

Significant results are obtained as shown in Figure 6, where the number of features has almost decreased to the half after using sequential forward floating feature selection. Figure 7 also shows impressing results in the perspective of accuracy. As shown in both figures, decreasing the number of features leads to higher accuracies in all cases, and that

Table 14: Comparison between 10-fold CV and LOPO CV for accelerometer, gyroscope, and EMG sensors after applying feature selection.

Classifier/validation protocol	10-fold CV (%)	LOPO CV (%)
Random forest	99.8	99.4
SVM	98	98.2
Decision tree	97.3	97.1
KNN	88.1	88.5

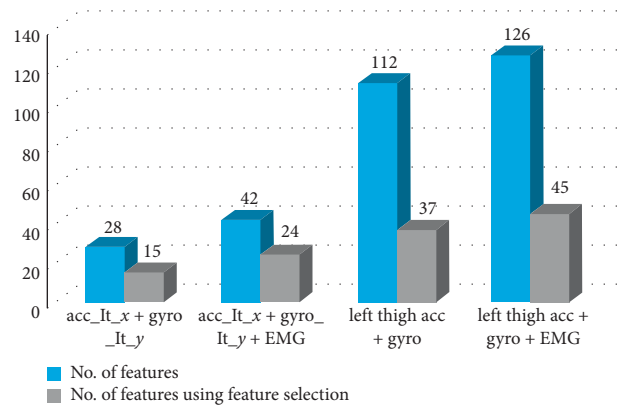

Figure 6: Difference in the number of features before and after using feature selection and sensor fusion.

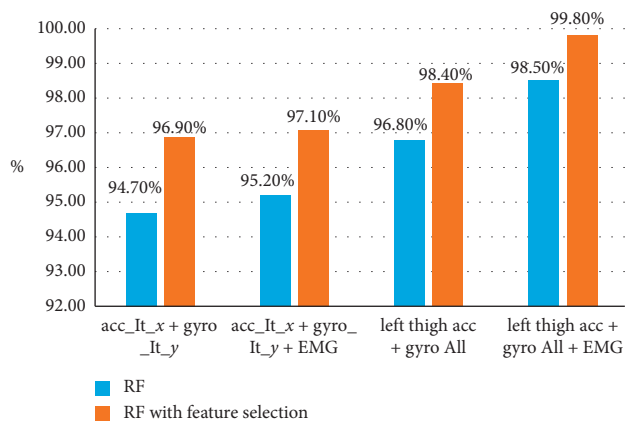

Figure 7: Difference in accuracies attained with and without feature selection as shown in Figure 6.

Table 15: List of input sources and the corresponding features acquired from them.

Input source	Features
A_lt_x	Jitter, mean, standard deviation, maximum, standard deviation auto covariance, standard deviation auto-correlation, and root-mean square
A_lt_y	Jitter, mean crossing rate, variance, minimum, maximum, standard deviation auto-correlation, kurtosis, and root-mean square
A_lt_z	Jitter, mean, standard deviation, minimum, variance, standard deviation auto covariance, skewness, and kurtosis
Ac_lt_mag	Mean and variance
G_lt_x G_lt_y	Mean, jitter, and standard deviation auto-correlation standard deviation, minimum, variance, mean auto correlation, root-mean square, and skewness
G_lt_z	Mean crossing rate, mean, mean auto covariance, and root-mean square
G_lt_mag	Mean crossing rate, standard deviation, standard deviation auto covariance, and root-mean square
EMG_l	Mean crossing rate, minimum, and kurtosis

occurs because the unnecessary information from the signal was removed automatically and only the informative features were kept to classify activates perfectly. Finally, Table 15 shows selected features after the fusion of the three sensor data; these features achieved an accuracy of 99.8% with the least number of features.

5. Conclusion

Towards accurate recognition of daily human activities, this paper proposed a novel approach that is based on sensor fusion and feature selection. Other than performing feature selection and sensor fusion consecutively, our pipeline learns a model that selects indicative features by jointly considering heterogeneous signals. These signals are acquired from electromyography and wearable inertial sensors on the thigh, foot, and shin. We believe that this approach enables constructive interaction between features that would have been dropped (during feature selection) otherwise. We attained a mean recognition accuracy of 99.8% on HuGaDB—the highest on this dataset—which provides signals from different sensor types (gyroscopes, accelerometers, and sEMG sensors), placements, and positions. Using off-the-shelf feature selection methods and time-based and statistical features, the presented joint fusion-selection approach had successfully realized the potential of sEMG sensors and incorporated them effectively to benefit the performance of the system. Moreover, towards the development of less obstructive systems, we highlighted the potential of the left thigh as a key sensor placement for attaining high recognition accuracies. A mean recognition accuracy of 98.4% was attained using only one inertial sensor on that single placement. Through extensive simulations and comparative analysis, we justified the impact of every stage in the proposed pipeline and showed the influence of various system parameters on the recognition accuracy. This research is envisaged to facilitate building robust systems that are tailored to specific scenarios and real-life applications.

Data Availability

Previously reported wearable inertial sensor and EMG sensor data (HuGaDB) were used to support this study and are available at DOI: 10.1007/978-3-319-73013-4_12. These prior studies (and datasets) are cited at relevant places within the text as references [4].

Conflicts of Interest

The authors declare no conflicts of interest.

Authors' Contributions

A.Al-Kabbany and H. Shaban carried out conceptualization, provided resources, and were responsible for supervision and project administration. A. Badawi, A. Al-Kabbany, and H. Shaban performed methodology, validation, formal analysis, investigation, reviewing and editing, and visualization; A. Badawi provided software and performed data curation. A. Badawi and A. Al-Kabbany wrote the original draft.

References

[1] M. Schwabacher and K. Goebel, "A survey of artificial intelligence for prognostics," Technical report, AAAI Fall Symposium, New York, NY, USA, 2007.

[2] M. Cornacchia, K. Ozcan, Y. Zheng, and S. Velipasalar, "A survey on activity detection and classification using wearable sensors," *IEEE Sensors Journal*, vol. 17, no. 2, pp. 386–403, 2017.

[3] E. De-La-Hoz-Franco, P. Ariza-Colpas, J. M. Quero, and M. Espinilla, "Sensor-based datasets for human activity recognition—a systematic review of literature," *IEEE Access*, vol. 6, pp. 59192–59210, 2018.

[4] R. Chereshnev, Kert'esz-Farkas, and A. Hugadb, "Human gait database for activity recognition from wearable inertial sensor networks," in *Proceedings of the International Conference on Analysis of Images, Social Networks and Texts*, pp. 131–141, Moscow, Russia, July 2017.

[5] A. Badawi, A. Al-Kabbany, and A. Shaban, "Multimodal human activity recognition from wearable inertial sensors using machine learning," in *Proceedings of the 2018 IEEE-EMBS Conference on Biomedical Engineering and Sciences (IECBES)*, pp. 402–407, Sarawak, Malasiya, December 2018.

[6] A. Badawi, A. Al-Kabbany, and A. Shaban, "Daily activity recognition using wearable sensors via machine learning and feature selection," in *Proceedings of the 2018 13th International Conference on Computer Engineering and Systems (ICCES)*, pp. 75–79, IEEE, Cairo, Egypt, December 2018.

[7] F.-C. Chuang, J. S. Wang, Y.-T. Yang, and T.-P. Kao, "A wearable activity sensor system and its physical activity classification scheme," in *Proceedings of the International Joint Conference on Neural Networks (IJCNN)*, IEEE, Brisbane, Australia, June 2012.

[8] N. C. Krishnan and S. Panchanathan, "Analysis of low resolution accelerometer data for continuous human activity recognition," in *Proceedings of the IEEE International Conference on Acoustics, Speech and Signal Processing*, IEEE, Las Vegas, NV, USA, April 2008.

[9] Y. J. Hong, I. J. Kim, S. C. Ahn, and H. G. Kim, "Activity recognition using wearable sensors for elder care," in *Proceedings of the Second International Conference on Future Generation Communication and Networking*, IEEE, Hainan, China, December 2008.

[10] L. Cheng, Y. Guan, K. Zhu, and Y. Li, "Recognition of human activities using machine learning methods with wearable sensors," in *Proceedings of the IEEE 7th Annual Computing and Communication Workshop and Conference (CCWC)*, IEEE, Las Vegas, NV, USA, March 2017.

[11] C. Tang and V. Phoha, "An empirical evaluation of activities and classifiers for user identification on smartphones," in *Proceedings of the 2016 IEEE 8th International Conference on Biometrics Theory, Applications and Systems (BTAS)*, pp. 1–8, IEEE, Niagara Falls, NY, USA, September 2016.

[12] S. H. Roy, M. S. Cheng, S.-S. Chang et al., "A combined sEMG and accelerometer system for monitoring functional activity in stroke," *IEEE Transactions on Neural Systems and Rehabilitation Engineering*, vol. 17, no. 6, pp. 585–594, 2009.

[13] H. Koskimäki, P. Siirtola, and J. Röning, "MyoGym: introducing an open gym data set for activity recognition collected using Myo armband," in *Proceedings of the2017 ACM International Joint Conference on Pervasive and Ubiquitous Computing and 2017 ACM International Symposium on Wearable Computers*, pp. 537–546, IEEE, Maui, Hawaiipp, September 2017.

[14] N. D. Nguyen, D. T. Bui, P. H. Truong, and G.-M. Jeong, "Position-based feature selection for body sensors regarding daily living activity recognition," *Journal of Sensors*, vol. 2018, Article ID 9762098, 13 pages, 2018.

[15] Q. Ni, L. Zhang, and L. Li, "A heterogeneous ensemble approach for activity recognition with integration of change point-based data segmentation," *Applied Sciences*, vol. 8, no. 9, p. 1695, 2018.

[16] K. Ku Abd Rahim, I. Elamvazuthi, L. Izhar, and G. Capi, "Classification of human daily activities using ensemble methods based on smartphone inertial sensors," *Sensors*, vol. 18, no. 12, p. 4132, 2018.

[17] Y.-J. Kim, Y. Kim, J. Ahn, and D. Kim, "Integrating hidden Markov models based on mixture-of-templates and k-NN2 ensemble for activity recognition," in *Proceedings of the 23rd International Conference on Pattern Recognition (ICPR)*, IEEE, Cancun, Mexico, pp. 1636–1641, December 2016.

[18] B. Chikhaoui and F. Gouineau, "Towards automatic feature extraction for activity recognition from wearable sensors: a deep learning approach," in *Proceedings of the IEEE ICDM Workshop on Data Mining for Aging, Rehabilitation and Independent Assisted Living*, New Orleans, LA, USA, November 2017.

[19] S. A. Khowaja, B. N. Yahya, and S.-L. Lee, "Hierarchical classification method based on selective learning of slacked hierarchy for activity recognition systems," *Expert Systems With Applications*, vol. 88, pp. 165–177, 2017.

[20] N. C. Krishnan and D. J. Cook, "Activity recognition on streaming sensor data," *Pervasive and Mobile Computing*, vol. 10, pp. 138–154, 2014.

[21] A. Jordao, A. C. Nazare, J. Sena, and W. Schwartz, "Human activity recognition based on wearable sensor data: a standardization of the state of the art," 2018, http://arxiv.org/abs/1806.05226.

[22] S. J. Preece, J. Y. Goulermas, L. P. J. Kenney, D. Howard, K. Meijer, and R. Crompton, "Activity identification using body-mounted sensors-a review of classification techniques," *Physiological Measurement*, vol. 30, no. 4, pp. R1–R33, 2009.

[23] P. Menschner, A. Prinz, P. Koene et al., "Reaching into patients' homes-participatory designed AAL service," *Electronic Markets*, vol. 21, pp. 63–76, 2011.

[24] S. Hemminki, P. Nurmi, and S. Tarkoma, "Accelerometer-based transportation mode detection on smartphones," in *Proceedings of the 11th ACM Conference on Embedded Networked Sensor Systems*, pp. 1–14, Association for Computing Machinery, Roma, Italy, November 2013.

[25] D. Figo, P. C. Diniz, D. R. Ferreira, and J. M. P. Cardoso, "Preprocessing techniques for context recognition from accelerometer data," *Personal and Ubiquitous Computing*, vol. 14, no. 7, pp. 645–662, 2010.

[26] D. Anguita, A. Ghio, L. Oneto, X. Parra, and J. L. Reyes-Ortiz, "A public domain dataset for human activity recognition using smartphones," in *Proceedings of the European Symposium on Artificial Neural Networks*, Bruges, Belgium, April 2013.

[27] P. Pudil, A. P. Somol, and M. Haindl, *Introduction to Statistical Pattern Recognition*, K. Fukunaga, Ed., Academic Press Professional, Inc., San Diego, CA, USA, 2013.

Hindawi
Journal of Healthcare Engineering
Volume 2020, Article ID 2802574, 7 pages
https://doi.org/10.1155/2020/2802574

Research Article

Dynamic Modeling and Simulation of a Body Weight Support System

Zhendong Song,[1] **Wei Chen**,[1] **Wenbing Wang**,[1] **and Guoqing Zhang**[2]

[1]*Shen Zhen Polytechnic, 4089 Shahe West Road, Shenzhen 518055, China*
[2]*People's Hospital of Gaoxin, 768 Fudong Road, Weifang 261205, China*

Correspondence should be addressed to Wei Chen; chenweil@szpt.edu.cn

Received 1 November 2019; Revised 18 December 2019; Accepted 2 January 2020; Published 12 February 2020

Academic Editor: João M. Tavares

This paper proposes a body weight support (BWS) system with a series elastic actuator (SEA) to facilitate walking assistance and motor relearning during gait rehabilitation. This system comprises the following: a mobile platform that ensures movement of the system on the ground, a BWS mechanism with an SEA that is capable of providing the desired unloading force, and a pelvic brace to smooth the pelvis motions. The control of the body weight support is realized by an active weight-offload method, and a dynamic model of the BWS system with offload mass of a human is conducted to simulate the control process and optimize the parameters. Preliminary results demonstrate that the BWS system can provide the desired support force and vertical motion of the pelvis.

1. Introduction

Based on the data of the World Health Organization in 2016, more than six million stroke survivors are disabled yearly [1]. Furthermore, stroke is a leading cause of serious long-term disability [2], and dyskinesia hinders gait training and rehabilitation [3]. A disability of the lower extremity limits functional independence in activities of daily living. Studies have shown that robot-assisted rehabilitation training is more effective than traditional gait training in improving walking ability in stroke patients [4], and body weight support (BWS) treadmill training is effective in enhancing patient mobility [5, 6]. During gait training, the pelvic vertical motion in the coronal plane plays an important role in the transformation between potential energy and kinetic energy, and hemiplegic patients need active mass-offloading to support their body weight. However, the guidance hypothesis in motor control research suggests that position-control-based movement might decrease motor learning for certain tasks [7]. Therefore, gait rehabilitation with flexible robots could help in providing the required dynamic force while also allowing for normal pelvic motions. Several robotic approaches have been developed to facilitate recovery based on the BWS system. Traditionally, an elastic spring [8], a winch [9], or a counterweight [10] with a wire harness is used in commercial BWS systems to relieve body weight.

However, the traditional BWS systems usually restrict the pelvis and trunk motion. Such a restriction is not beneficial to balance recovery. Thus, active BWS systems with pelvic support and novel control algorithm were studied as shown in Figure 1. A height-adjustable saddle was employed in the Pacer Gait Trainers of Rifton Equipment Co., Ltd. to assist gait training [11], and a pneumatic pusher was used to provide mass-offloading. GaitEnable [12], Robotic Walker [13], and Kineassist [14] can provide patients with active BWS and part of passive pelvic motions by using a linear actuator and pelvic brace. The balance assessment robot (BAR) with four linear actuators and interaction force sensors was developed by Olenšek et al. [15] to control the pelvic position and orientation. The BAR can monitor the support force and provide adjustments in real time. In addition, a wire-driven pelvic support mechanism, namely, tethered pelvic assist device (TPAD), was developed by Kang

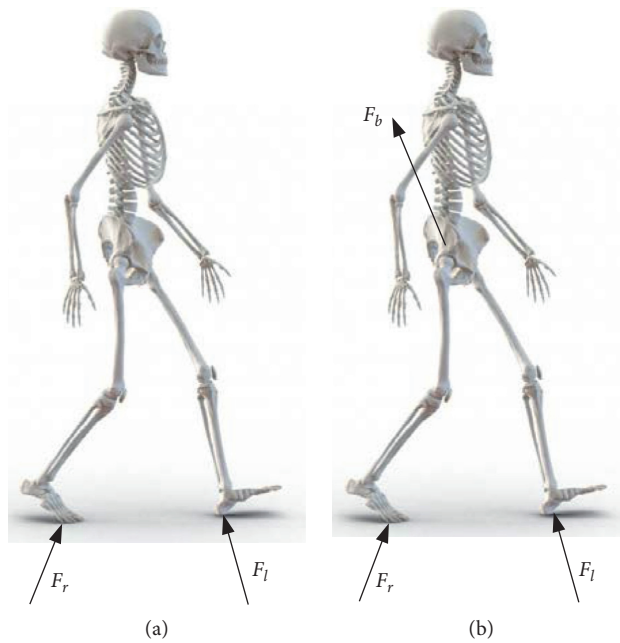

Figure 1: Forces acting on a human during gait: normal gait (a) without BWS and (b) with BWS.

et al. [16]. The TPAD can guide the pelvic motions by controlling the interaction forces acting on the pelvis. However, the active BWS series elastic actuators (SEAs) are often considered to improve training safety. Thus, a pelvic support robot with BWS was developed and active BWS was provided for the vertical motion of the pelvis.

The rest of the paper is organized as follows. Section 2 contains a description of the robot. Section 3 describes the modeling and controller design of the system. Section 4 presents the MATLAB/Simulink simulation and discussion. Finally, Section 5 provides conclusions and future work.

2. System Description

A BWS system generally works in conjunction with a treadmill or a mobile platform (MP) to achieve gait training. Compared with the treadmill, the advantages of the MP are as follows: (1) the training environment is realistic, and the participants can feel the acceleration of the center of mass (CoM); (2) family rehabilitation training could be realized in this platform with a small MP. Therefore, a robot comprising a mobile platform, a BWS system, and a pelvic brace was designed as shown in Figure 2.

2.1. Robot Design. The overall conceptualized design and the prototype of the robot are shown in Figure 2. Three force sensors are used to identify the motion intention, and then the computer controls the motor of the BWS to support the body weight and two driving wheels to follow human motions. The modeling and control of the BWS are mainly discussed in this study.

The MP mainly aims at providing over-ground mobility, thereby achieving the gait rehabilitation training. The MP comprises two active wheels to provide power, two passive castors to maintain balance, and a U-shaped rigid steel frame. Based on the motions of the lower limbs, the U-shaped rigid steel frame is designed to satisfy approximately 0.8 and 1.2 m of free space in the medial/lateral and the anterior/posterior directions, respectively. The rotation of the robot is realized by the differential driving of the two wheels.

The BWS driven by a servo motor is designed to achieve the vertical displacement of the pelvis (approximately 0.2 m) and provide subjects with appropriate BWS via a guide screw and a set of linear guideways. A force sensor is installed to measure the interaction force between the robot and the human. A set with a ball spline and two springs is installed to achieve accurate force control and facilitate comfortable interaction with the robot. This part is used to reduce the undesirable forces generated by the control lag. The system control is implemented in TwinCAT2 using a controller (Beckhoff PLC CX5130). Based on the error between the desired and the interaction forces, the servo motor generates the corresponding dynamic force to support the human body weight.

A pelvic brace is designed to smooth the pelvic motions and install the force sensors. A pelvic brace is designed based on the range of pelvic motions during normal gait to achieve pelvic obliquity and rotation. A force sensor is installed between the BWS and the pelvic brace, and then a revolute pair is used to achieve pelvic obliquity. Afterward, a pair of cambered slideway is used to achieve pelvic rotation. At the end of the pelvic brace, two pressure sensors are installed, and the force signal is used to identify the motion intentions of the users.

2.2. Problem Statement. During bipedal walking with a treadmill, the interchange between kinetic energy and potential energy is a continuous process, and the vertical

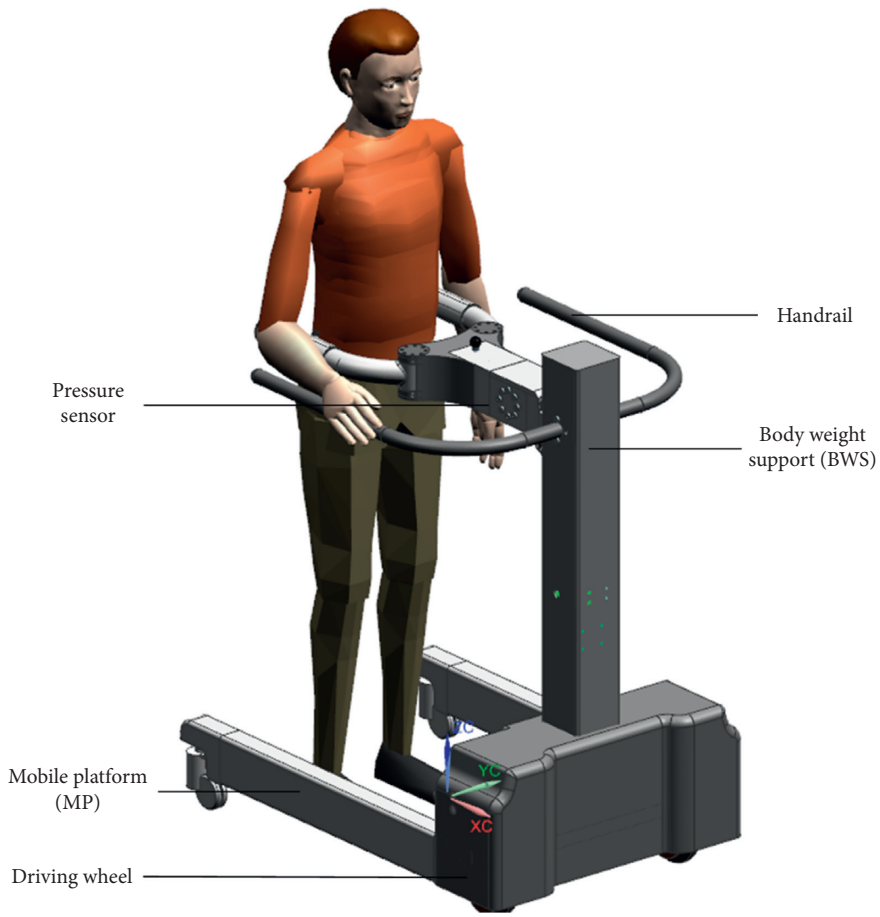

Figure 2: CAD model of the system.

motion of the CoM is crucial in this process [17]. However, for the BWS, the vertical motion is unfavorable for the constant value of the mass-offloading, particularly for the passive BWS systems with counterweights, winches, or springs. Thus, the active BWS systems are developed to improve the offloading accuracy and dynamic performance of the BWS [18–22]. However, the existing rigid BWS systems usually generate undesirable forces and rigid impacts due to the existence of control lag and inertia. Meanwhile, the force-control-based strategies are used to provide users with appropriate force assistance to guide the pelvic movements. Thus, the SEA BWS is used to control the robot.

3. Modeling and Control

3.1. Dynamic Model. The kinematics model of the rehabilitation robot is shown in Figure 3, where OXYZ is the global coordinate system, point E is the midpoint of two passive castors, and $o_0x_0y_0z_0$ is the local coordinate system attached to the robot. The BWS system is located at point E, through the pelvic brace connected to the pelvic center O_p, and point C is the mass center of the rehabilitation robot. Using the position, orientation and velocity of point E to, respectively, indicate the position, orientation, and velocity of the robot, θ is the heading angle of the mobile platform

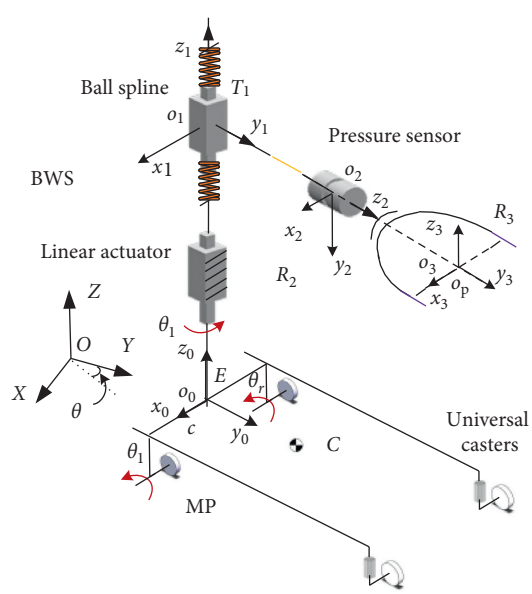

Figure 3: Schematic of the system.

relative to the X-axis. $2c$ is the distance between the two driving wheels, a is the distance from point E to pelvic center projected to Oxy, r is the radius of driving wheel, and d is the distance from the mass center C to the reference point E.

The velocity matrix of the MP relative to the global coordinate system is defined as $\dot{\mathbf{q}} = \left[\dot{x}\ \ \dot{y}\ \ \dot{\theta}\right]^{\mathbf{T}}$, angular velocity of two driving wheels as $\boldsymbol{\omega} = \left[\dot{\theta}_l\ \ \dot{\theta}_r\right]^{\mathbf{T}}$, and the velocity matrix relative to a local coordinate system as $\dot{\mathbf{q}}_R = \left[\dot{x}_R\ \ \dot{y}_R\ \ \dot{\theta}_R\right]^{\mathbf{T}}$. Under the circumstances that the kinestate of driving wheels is pure rolling without sliding and the mobile platform can perform instantaneous motion along heading direction of the driving wheels, kinematics equation of the robot can be obtained based on the following geostatistics:

$$\dot{\mathbf{q}}_R = \begin{bmatrix} \frac{r}{2} & \frac{r}{2} \\ 0 & 0 \\ \frac{r}{2c} & -\frac{r}{2c} \end{bmatrix} \begin{bmatrix} \dot{\theta}_l \\ \dot{\theta}_r \end{bmatrix}. \tag{1}$$

By taking point E as a reference point, equation (5) premultiplies the rotation matrix and $\dot{q}_R$ translates to robot velocity in a global coordinate system:

$$\dot{\mathbf{q}} = \begin{bmatrix} \cos\theta & 0 & -e\sin\theta \\ \sin\theta & 0 & e\cos\theta \\ 0 & 0 & 1 \end{bmatrix} \dot{q}_R. \tag{2}$$

For the control of the MP, speed control is used to follow the motion on the ground. Meanwhile, torque control is utilized to control the BWS system to provide accurate offloading for users. Thus, the dynamic model is calculated.

The estimated value of the sensor is used to replace the actual value, to put the theoretical model into a simulated program as shown in Figure 4, and then the interaction force can be expressed as follows:

$$F_h = \frac{(k_s\theta_s)}{l}, \tag{3}$$

where k_s is the elastic coefficient of the torque sensor, $l = \|\overrightarrow{o_sP_0}\|$ is the distance from the sensor to the pelvic center, and θ_s is the deformation of the sensor, which can be expressed as follows:

$$\theta_s = 2\sin^{-1}\left(\frac{z_h - z_p}{2l}\right), \tag{4}$$

where z_h is the position of pelvic center and z_p is the z-axis component of the mass center of M_p, that is, the center of the ball spline. Based on the Newton–Euler method, the equilibrium equation of M_p can be expressed as follows:

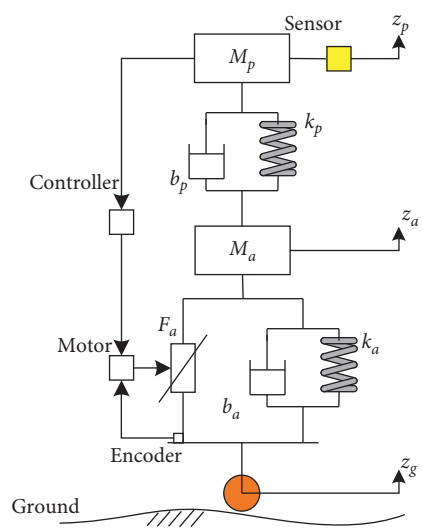

Figure 4: Mass-spring-damper system of the BWS.

$$F_h + b_p\left(\dot{z}_p - \dot{z}_a\right) + k_p\left(z_p - z_a\right) + M_p\, g + M_h g = M_p\ddot{z}_p, \tag{5}$$

where b_p is the viscosity coefficient of the ball spline, k_p is the elastic coefficient of the spring, M_h is the mass of the pelvic brace, z_a is the z-axis component position of the guide screw, $\dot{z}_a$ is the velocity of the guide screw, $\dot{z}_p$ is the velocity of the ball spline, $\ddot{z}_p$ is the acceleration of the ball spline, and g is the gravitational constant. Then, $\ddot{z}_p$ can be obtained as follows:

$$\ddot{z}_p = \frac{F_h + b_p\left(\dot{z}_p - \dot{z}_a\right) + k_p\left(z_p - z_a\right) + M_p g + M_h g}{M_p}. \tag{6}$$

The equilibrium equation of M_a for the guide screw can be expressed as follows:

$$F_a + b_p\left(\dot{z}_p - \dot{z}_a\right) + k_p\left(z_p - z_a\right) + b_a\left(\dot{z}_a - \dot{z}_g\right) + k_a\left(z_a - z_g\right) + M_a g = M_a\ddot{z}_a, \tag{7}$$

where F_a is the desired force, b_a is the viscosity coefficient of the guide screw, k_a is the elastic coefficient of the guide screw, z_g is the z-axis component of the driving wheel, $\dot{z}_g$ is the velocity of the driving wheel, and $\ddot{z}_a$ is the acceleration of the guide screw. Then, $\ddot{z}_a$ can be obtained as follows:

$$\ddot{z}_a = \frac{F_a + b_p\left(\dot{z}_p - \dot{z}_a\right) + k_p\left(z_p - z_a\right) + b_a\left(\dot{z}_a - \dot{z}_g\right) + k_a\left(z_a - z_g\right) + M_a g}{M_a}. \tag{8}$$

By combining equations (3)–(7), the dynamic equation of the BWS system can be obtained as follows:

$$\tau_c = M\ddot{q} + B(q, \dot{q}) + J^T F_v, \tag{9}$$

where τ_c is the desired torque of motor; M is the generalized mass; $B(q, \dot{q})$ is the generalized Coriolis, centrifugal, and external forces, including the gravity forces; $\ddot{q}$ is the generalized acceleration; F_v is the offloading; and J^T is the configuration-dependent Jacobian matrix. The transformation relationship from the desired force to the desired torque can be expressed as follows:

$$\tau_c = \frac{F_a L}{2\pi\eta} + I_m \ddot{\theta}_m, \tag{10}$$

where L is the helical pitch of the guide screw, η is the transmission efficiency, I_m is the inertia of the motor, and $\ddot{\theta}_m$ is the angular acceleration of the motor.

3.2. Torque Control. The control algorithm of the robot is divided into two control levels: (1) high-level controller and (2) low-level controller. The task of the high-level controller is to recognize the motion intention of the user. Figure 5 shows that the task of the low-level controller is to filter the input signals and output the appropriate torque. The low-level and high-level controllers are executed at 1000 and 100 Hz, respectively.

The goal of the torque controller is to provide the user with stable mass-offloading, and the control architecture of the BWS system is shown in Figure 5. F_v is the desired value of offloading, and F_h is the input signal from the torque sensor, that is, the interaction force. When the user walks on the ground, the vertical motion of the pelvis will result in the change in input signal, and then the controller will generate torque to decrease the error between the desired and interaction forces. The torque controller with double-layer PID and the dynamic term is then given by the following equation:

$$\begin{aligned} e &= F_v - F_h, \\ \dot{e} &= \dot{F}_v - \dot{F}_h, \\ \tau_a &= M\ddot{q} + B(q, \dot{q}) + J^T F_v + K_p e + K_d \dot{e} + K_i \int e \, dt, \end{aligned} \tag{11}$$

where e is the error between desired offloading and observed force, and the gain matrices for the first layer PID controller are provided by K_p, K_d, and K_i. The goal of the second layer PID is to ensure that the output torque is coincident with the desired torque.

4. Simulation and Verification

Simulation studies were conducted in this paper to verify the effectiveness of the proposed control method. The MATLAB/Simulink was used in the simulation to simulate the processes of the BWS with the proposed method.

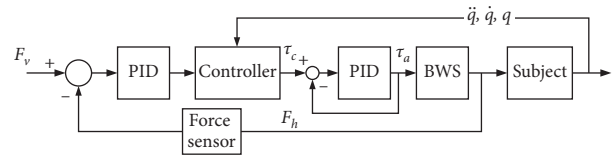

Figure 5: Control architecture of the system.

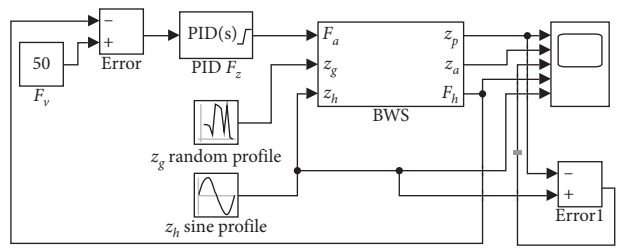

Figure 6: Simulation block diagram in MATLAB/Simulink.

Table 1: Inertial properties of links.

Link	Masses (kg)	Position vector of CG (m)
1 (T)	50	0.55
2 (R)	8	0.15
3 (R)	15	0.2

4.1. Simulation. The simulation block diagram is shown in Figure 6. In the simulation process, the z-axis component of the driving wheel (z_g) was a random profile block, and the vertical motion of the pelvis (z_h) was assumed as a sine profile block. The "BWS" block was the compute module based on equations (3)–(7), and the solver was ode45. Two different cases of offloading, namely, 0.0 N and 150.0 N, were simulated in this paper. The parameters of the PID were adjusted during the simulation to achieve the desired characteristics. The conditions of the aforementioned trials are summarized in Table 1. The simulation results are shown in Figures 7 and 8. The simulation values, desired values, and the error between the simulation and desired forces for the case of 0.0 N offloading are given in Figure 7. Meanwhile, the simulation values, desired values, and the simulation force for the case of 150.0 N offloading are given in Figure 8.

As shown in Figure 7, the controller updated the desired torque during the gait cycle to follow the position of the pelvic center, while the torque controller was used to ensure the mass-offloading. The changed simulation values resembled the desired values with small steady-state error during the simulation, and the steady-state error of offloading was less than 2 N. This phenomenon demonstrated the capability to track dynamical parameters. Figure 8 shows that the controller was used to track the position of the pelvic center and provide 150.0 N offloading during the gait cycle. The changed simulation values resembled the desired values during the simulation, but the position error was approximately 0.025 m mainly due to the stiffness of the force sensor. The mean error of

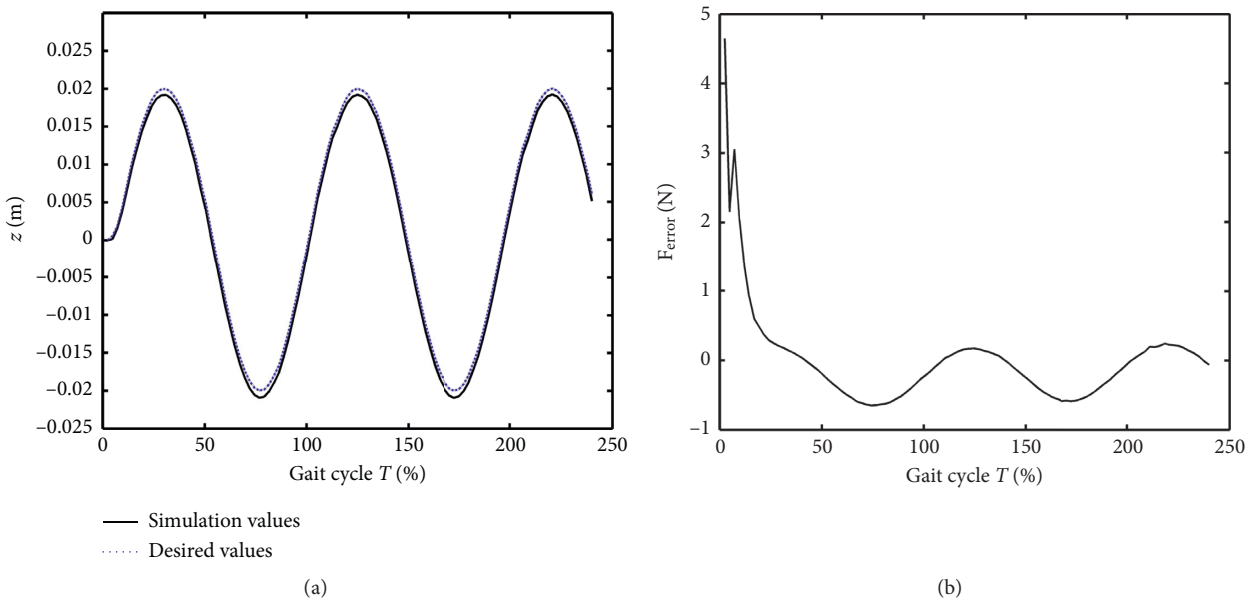

Figure 7: Simulation results with 0 kg offloading. (a) Vertical position of pelvic center. (b) Force error.

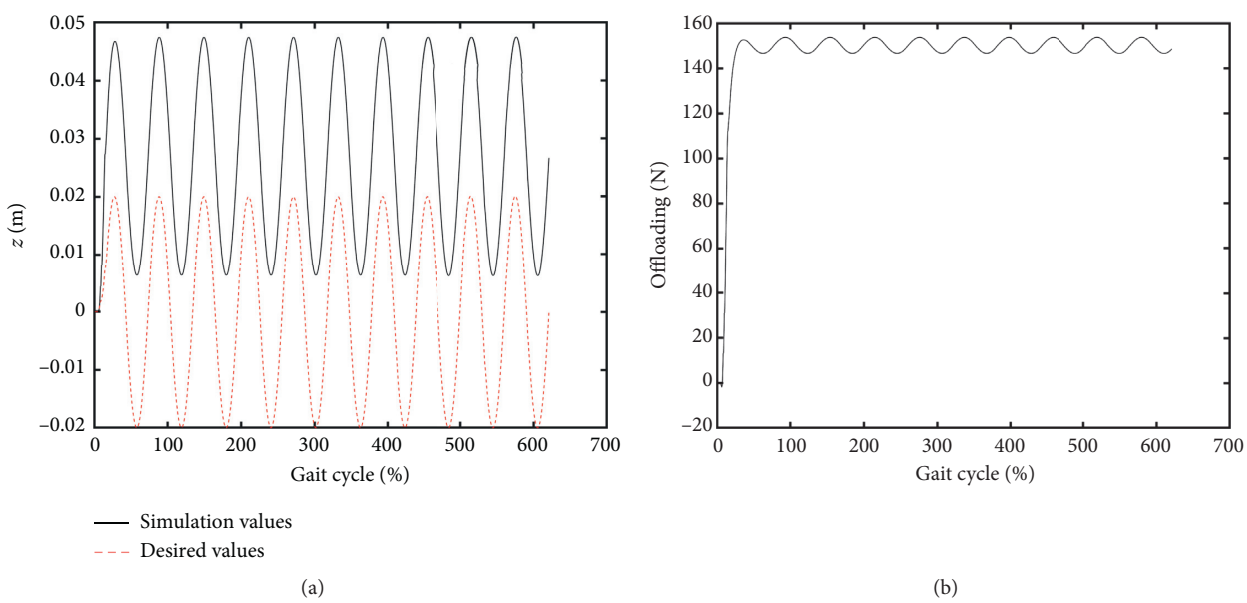

Figure 8: Simulation results with 15 kg offloading. (a) Vertical position of pelvic center. (b) Offloading force.

offloading was less than 3.1 N, demonstrating the capability to track dynamical parameters.

4.2. Discussion. The simulation results show that the proposed method was capable of providing the desired mass-offloading with small steady-state error, but the position tracking must consider the stiffness of the force sensor. Less time is needed to achieve a stable state when using the PID controller. Furthermore, the parameters of the PID must adjust to achieve the desired characteristics with different cases of the mass-offloading. The system inertia is increased with the mass-offloading. Therefore, the PID parameters must be adjusted to provide the desired mass-offloading.

5. Conclusion

This paper introduces a novel robotic BWS device for disabled people to conduct rehabilitation training. The present work also demonstrates the potential capability of a novel BWS system. Dynamic modeling and control algorithms are proposed based on the design concept to optimize the control of the interaction force. The preliminary simulation verification with MATLAB simulation is conducted to prove the effectiveness of the control algorithm. The BWS system

may be used to improve the pelvic control function of stroke survivors. Furthermore, the robot will be fabricated, and the control algorithm of mass-offloading will be studied in the future.

Data Availability

The simulation results and experimental results data used to support the findings of this study are available from the corresponding author upon request.

Conflicts of Interest

The authors declare that they have no conflicts of interest.

Acknowledgments

This work was supported by Youth Innovative Project of Guangdong Education Department under Grant 6019210033K.

References

[1] J. Walter, O. Oyere, O. Mayowa, and S. Sonal, "Stroke: a global response is needed," *Bulletin of the World Health Organization*, vol. 94, no. 9, p. 634, 2016.

[2] L. Bizovska, Z. Svoboda, and M. Janura, "The possibilities for dynamic stability assessment during gait: a review of the literature," *Journal of Physical Education & Sport*, vol. 15, no. 3, pp. 490–497, 2015.

[3] S. A. Combos, E. L. Dugan, M. Passmore, C. Riesner, D. Whipker, and E. Yingling, "Balance, balance confidence, and health related quality of life in persons with chronic stroke after body weight-supported treadmill training," *Archives of Physical Medicine and Rehabilitation*, vol. 91, no. 12, pp. 1914–1919, 2010.

[4] H. Erika, E. Christina, T. Lin et al., "Robot-applied resistance augments the effects of body weight-supported treadmill training on stepping and synaptic plasticity in a rodent model of spinal cord injury," *Neurorehabilitation and Neural Repair*, vol. 31, no. 8, pp. 746–757, 2017.

[5] F. Sylos-Labini, F. Lacquaniti, and Y. P. Ivanenko, "Human locomotion under reduced gravity conditions: biomechanical and neurophysiological considerations," *BioMed Research International*, vol. 2014, no. 23, 12 pages, 2014.

[6] S. Hesse, C. Bertelt, M. T. Jahnke et al., "Treadmill training with partial body weight support compared with physiotherapy in nonambulatory hemiparetic patients," *Stroke*, vol. 26, no. 6, pp. 976–981, 1995.

[7] P. Agarwal, Y. Yun, J. Fox, K. Madden, and A. D. Deshpande, "Design, control, and testing of a thumb exoskeleton with series elastic actuation," *The International Journal of Robotics Research*, vol. 36, no. 3, pp. 355–375, 2017.

[8] X. Liu, A. Rossi, and I. Poulakakis, "SPEAR: a monopedal robot with switchable parallel elastic actuation," in *Proceedings of the IEEE/RSJ International Conference on Intelligent Robots & Systems*, Hamburg, Germany, October 2015.

[9] A. A. A. Braidot and G. L. Aleman, "Design of a mechanical system in gait rehabilitation with progressive addition of weight," *Journal of Physics: Conference Series*, vol. 332, no. 1, Article ID 012045, 2011.

[10] F. Gazzani, A. Fadda, M. Torre, and V. Macellari, "WARD: a pneumatic system for body weight relief in gait rehabilitation," *IEEE Transactions on Rehabilitation Engineering*, vol. 8, no. 4, pp. 506–513, 2000.

[11] Pacer Gait Trainers, 2018, https://www.rifton.com/.

[12] A. Morbi, M. Ahmadi, and A. Nativ, "GaitEnable: an omnidirectional robotic system for gait rehabilitation," in *Proceedings of the 2012 International Conference on Mechatronics & Automation*, pp. 936–941, Chengdu, China, August 2012.

[13] K.-R. Mun, S. B. Lim, Z. Guo, and H. Yu, "Biomechanical effects of body weight support with a novel robotic walker for over-ground gait rehabilitation," *Medical & Biological Engineering & Computing*, vol. 55, no. 2, pp. 315–326, 2017.

[14] J. Patton, D. A. Brown, M. Peshkin et al., "KineAssist: design and development of a robotic overground gait and balance therapy device," *Topics in Stroke Rehabilitation*, vol. 15, no. 2, pp. 131–139, 2008.

[15] A. Olenšek, M. Zadravec, and Z. Matjačić, "A novel robot for imposing perturbations during overground walking: mechanism, control and normative stepping responses," *Journal of Neuroengineering and Rehabilitation*, vol. 13, no. 1, p. 55, 2016.

[16] J. Kang, V. Vashista, and S. K. Agrawal, "On the adaptation of pelvic motion by applying 3-dimensional guidance forces using TPAD," *IEEE Transactions on Neural Systems and Rehabilitation Engineering*, vol. 25, no. 9, pp. 1558–1567, 2017.

[17] J. Ye, Y. Nakashima, B. Zhang et al., "Functional electrical stimulation based on a pelvis support robot for gait rehabilitation of hemiplegic patients after stroke," in *Proceedings of the International Conference of the IEEE Engineering in Medicine and Biology Society*, pp. 3098–3101, Chicago, IL, USA, August 2014.

[18] Q. Lu, J. Liang, B. Qiao, and O. Ma, "A new active body weight support system capable of virtually offloading partial body mass," *IEEE/ASME Transactions on Mechatronics*, vol. 18, no. 1, pp. 11–20, 2013.

[19] J. Mignardot, C. G. Goff, R. V. Den Brand et al., "A multidirectional gravity-assist algorithm that enhances locomotor control in patients with stroke or spinal cord injury," *Science Translational Medicine*, vol. 9, no. 399, Article ID eaah3621, 2017.

[20] T. Watanabe, E. Ohki, T. Ando et al., "Fundamental study of force control method for pelvis-supporting body weight support system," in *Proceedings of the IEEE International Conference on Robotics and Biomimetics*, pp. 1403–1408, Bangkok, Thailand, February 2009.

[21] A. Moseley, A. Stark, I. Cameron, and A. Pollock, "Selection treadmill training and body weight support for walking after stroke," *Physiotherapy*, vol. 89, no. 9, p. 515, 2003.

[22] H. Munawar and V. Patoglu, "Gravity-assist: a series elastic body weight support system with inertia compensation," in *Proceedings of the IEEE/RSJ International Conference on Intelligent Robots & Systems*, IEEE, Daejeon, South Korea, October 2016.